

1

2

3 **Tuning site-specific dynamics to drive allosteric activation in a pneumococcal**
4 **zinc uptake regulator**

5

6 Daiana A. Capdevila,[†] Fidel Huerta,^{†,‡} Katherine A. Edmonds,[†] My T. Le,[†] Hongwei Wu,[†] and
7 David P. Giedroc^{*,†,§}

8

9 [†]*Department of Chemistry*, Indiana University, 800 E. Kirkwood Drive, Bloomington, IN 47405-
10 7102, United States

11 [‡]*Graduate Program in Biochemistry*, Indiana University, 212 S. Hawthorne Drive, Bloomington,
12 IN 47405, United States

13 [§]*Department of Molecular and Cellular Biochemistry*, Indiana University, 212 S. Hawthorne
14 Drive, Bloomington, IN 47405 United States

15

16 *Correspondence to David P. Giedroc*: giedroc@indiana.edu

17

18 **Abstract**

19 MarR (multiple antibiotic resistance repressor) family proteins are bacterial repressors that
20 regulate transcription in response to a wide range of chemical signals.
21 Although specific features of MarR family function have been described, the role of atomic
22 motions in MarRs remains unexplored thus limiting insights into the evolution of allostery in this
23 ubiquitous family of repressors. Here, we provide the first experimental evidence that internal
24 dynamics play a crucial functional role in MarR proteins. *Streptococcus pneumoniae* AdcR
25 (adhesin-competence repressor) regulates Zn^{II} homeostasis and Zn^{II} functions as an allosteric
26 activator of DNA binding. Zn^{II} coordination triggers a transition from independent domains to a
27 more compact structure. We identify residues that impact allosteric activation on the basis of
28 Zn^{II}-induced perturbations of atomic motions over a wide range of timescales. These findings
29 reconcile the distinct allosteric mechanisms proposed for other MarRs and highlight the
30 importance of conformational dynamics in biological regulation.

31

32

33

34 **Introduction**

35 Successful bacterial pathogens respond to diverse environmental insults or changes in
36 intracellular metabolism by modulating gene expression (Alekshun & Levy, 2007). Such
37 changes in gene expression are often mediated by “one-component” transcriptional regulators,
38 which directly sense chemical signals and convert such signals into changes in transcription.
39 Members of the multiple antibiotic resistance regulator (MarR) family are critical for the survival
40 of pathogenic bacteria in hostile environments, particularly for highly antibiotic-resistant
41 pathogens (Ellison & Miller, 2006, Yoon *et al.*, 2009, Weatherspoon-Griffin & Wing, 2016,
42 Tamber & Cheung, 2009, Aranda *et al.*, 2009, Grove, 2017). Chemical signals sensed by MarRs
43 include small molecule metabolites (Deochand & Grove, 2017), reactive oxygen species (ROS)
44 (Liu *et al.*, 2017, Sun *et al.*, 2012) and possibly reactive sulfur species (RSS) (Peng *et al.*, 2017).
45 It has been proposed that evolution of new MarR proteins enables micro-organisms to colonize
46 new niches (Deochand & Grove, 2017), since species characterized by large genomes and a
47 complex lifestyle encode many, and obligate parasitic species with reduced genome sizes encode
48 few (Perez-Rueda *et al.*, 2004). Therefore, elucidating how new inducer specificities and
49 responses have evolved in this ubiquitous family of proteins on what is essentially an unchanging
50 molecule scaffold is of great interest, as is the molecular mechanism by which inducer binding or
51 cysteine thiol modification allosterically regulates DNA operator binding in promoter regions of
52 regulated genes.

53 Obtaining an understanding of how allostery has evolved in one-component regulatory
54 systems (Ulrich *et al.*, 2005, Marijuan *et al.*, 2010), including MarR family repressors, requires a
55 comprehensive analysis of the structural and dynamical changes that occur upon inducer and
56 DNA binding (Capdevila *et al.*, 2017a, Tzeng & Kalodimos, 2013, West *et al.*, 2012, Tzeng &
57 Kalodimos, 2009). For MarRs, several distinct allosteric mechanisms have been proposed, from

58 a “domino-like” response (Bordelon *et al.*, 2006, Gupta & Grove, 2014, Perera & Grove, 2010)
59 to ligand binding-mediated effects on asymmetry within the dimer (Anandapadamanaban *et al.*,
60 2016), to oxidative crosslinking of *E. coli* MarR dimers into DNA binding-incompetent tetramers
61 (Hao *et al.*, 2014). While there are more than 130 crystal structures of MarR family repressors in
62 different allosteric states (Fig. S1), an understanding of the role of atomic motions and the
63 conformational ensemble in MarRs is nearly totally lacking and what is known is based
64 exclusively on simulations (Anandapadamanaban *et al.*, 2016, Sun *et al.*, 2012). Here, we
65 provide the first experimental evidence in solution that internal dynamics play a crucial
66 functional role in a MarR protein, thus define characteristics that may have impacted the
67 evolution of new biological outputs in this functionally diverse family of regulators.

68 In the conventional regulatory paradigm, the binding of a small molecule ligand, or the
69 oxidation of conserved ROS-sensing cysteines induces a structural change in the homodimer that
70 typically negatively impacts DNA binding affinity. This results in a weakening or dissociation
71 of the protein-DNA complex and transcriptional derepression. Several reports provide evidence
72 for a rigid body reorientation of the two α 4 (or α R)-reading heads within the dimer (Fig. 1A-B,
73 Fig. S1) (Alekshun *et al.*, 2001, Fuangthong & Helmann, 2002, Wilke *et al.*, 2008, Chang *et al.*,
74 2010, Liu *et al.*, 2017, Deochand & Grove, 2017, Dolan *et al.*, 2011, Deochand *et al.*, 2016).
75 The generality of this simple paradigm is inconsistent with the findings that some MarR proteins
76 share very similar static structures in the active (DNA binding-competent) and inactive (DNA
77 binding-incompetent) states (Anandapadamanaban *et al.*, 2016, Kim *et al.*, 2016, Liguori *et al.*,
78 2016); furthermore, several active states have been shown to require a significant rearrangement
79 to bind DNA (Alekshun *et al.*, 2001, Liu *et al.*, 2017, Zhu *et al.*, 2017b, Hao *et al.*, 2013, Gao *et*
80 *al.*, 2017, Chin *et al.*, 2006, Saridakis *et al.*, 2008). In fact, a comprehensive analysis of all
81 available MarR family structures strongly suggests that the degree of structural reorganization

82 required to bind DNA, characterized by a narrow distribution of α 4- α 4' orientations, is
83 comparable whether transitioning from the inactive *or* active states of the repressor (Fig. 1C,
84 Table S1). These observations strongly implicate a conformational ensemble model of allosteric
85 (Motlagh *et al.*, 2014) (Fig. 1B-D), where inducer sensing impacts DNA binding by restricting
86 the conformational spread of the active repressor, as was proposed in a recent molecular
87 dynamics study (Anandapadamanaban *et al.*, 2016).

88 MarR proteins are obligate homodimers that share a winged-helical DNA-binding
89 domain connected to a DNA-distal all-helical dimerization domain where organic molecules
90 bind in a cleft between the two domains (Fig. S1B). Individual MarR members have been shown
91 to bind a diverse range of ligands at different sites on the dimer (Otani *et al.*, 2016, Takano *et al.*,
92 2016); likewise, oxidation-sensing cysteine residues are also widely distributed in the dimer
93 (Fuangthong & Helmann, 2002, Liu *et al.*, 2017, Hao *et al.*, 2014, Dolan *et al.*, 2011, Chen *et al.*,
94 2006). This functional diversity is accompanied by relatively low overall sequence similarity,
95 which suggests that a conserved molecular pathway that connects sensing sites and the DNA
96 binding heads is highly improbable. Complicating our current mechanistic understanding of this
97 family is that for many members, including *E. coli* MarR, the physiological inducer (if any) is
98 unknown, rendering functional conclusions on allosteric from crystallographic experiments alone
99 less certain (Hao *et al.*, 2014, Zhu *et al.*, 2017b).

100 In contrast to the extraordinary diversity of thiol-based switching MarRs, MarR family
101 metallosensors are confined to a single known regulator of Zn^{II} uptake, exemplified by AdcR
102 (adhesin competence regulator) from *S. pneumoniae* and closely related *Streptococcus* spp. (Loo
103 *et al.*, 2003, Reyes-Caballero *et al.*, 2010) and ZitR from *Lactococcus* spp (Llull *et al.*, 2011,
104 Zhu *et al.*, 2017c). AdcR and ZitR both possess two closely spaced pseudotetrahedral Zn^{II}
105 binding sites termed site 1 and site 2 (Fig. 1A) that bind Zn^{II} with different affinities (Reyes-

106 Caballero *et al.*, 2010, Guerra *et al.*, 2011, Sanson *et al.*, 2015, Zhu *et al.*, 2017c). Zn^{II} is an
107 allosteric *activator* of DNA operator binding which is primarily dependent on the structural
108 integrity of site 1 (Reyes-Caballero *et al.*, 2010, Zhu *et al.*, 2017c). ZitR has been recently
109 extensively structurally characterized, with crystallographic models now available for the apo-
110 and Zn^{II}₁- (bound to site 1) and Zn^{II}₂- and Zn^{II}₂-DNA operator complexes, thus providing
111 significant new insights into ZitR and AdcR function (Zhu *et al.*, 2017c). These structures reveal
112 that Zn^{II}₂-ZitR and Zn^{II}₂-AdcR form triangularly-shaped homodimers and are essentially
113 identical, as anticipated from their high sequence identity (49%). Apo-ZitR adopts a
114 conformation that is incompatible with DNA binding, and filling of both Zn^{II} sites is required to
115 adopt a conformation that is similar to that of the DNA-complex. Thermodynamically, filling of
116 the low affinity site 2 enhances allosteric activation of DNA-binding by \approx 10-fold, and this occurs
117 concomitant with a change in the H42 donor atom to the site 1 Zn^{II} ion from N ϵ 2 in the apo- and
118 Zn^{II}₁-states to N δ 1 in the Zn^{II}₂-ZitR (as in Zn^{II}₂ AdcR; (Guerra *et al.*, 2011)) and Zn^{II}₂ ZitR-DNA
119 operator complexes (Zhu *et al.*, 2017c). Allosteric *activation* by Zn^{II} is in strong contrast to all
120 other members of the MarR superfamily, consistent with its biological function as uptake
121 repressor at high intracellular Zn^{II}.

122 Here we employ a combination of NMR-based techniques and small angle x-ray
123 scattering (SAXS) to show that apo- (metal-free) AdcR in solution is characterized by multiple
124 independent domains connected by flexible linkers, resulting in a distinct quaternary structure
125 from the Zn-bound state previously structurally characterized (Guerra *et al.*, 2011). Our
126 backbone relaxation dispersion-based NMR experiments show that apo-AdcR samples distinct
127 conformational states in the μ s-ms timescale, while Zn^{II} narrows this distribution by
128 conformational selection, increasing the population of a state that has higher affinity for DNA.
129 This finding is fully consistent with the crystallographic structures of Zn^{II}₂ ZitR and the Zn^{II}₂

130 ZitR:DNA complex (Zhu *et al.*, 2017c). The site-specific backbone and methyl sidechain
131 dynamics in the ps-ns timescale show that Zn^{II} not only induces a general restriction of these
132 protein dynamics, but also enhances fast timescale, low-amplitude motions in the DNA binding
133 domains. Together, these data reveal that Zn^{II} coordination promotes a conformational change
134 that reduces the entropic cost of DNA binding and enhances internal dynamics uniquely within
135 the DNA binding domain, thus poised the repressor to interact productively with various DNA
136 operator target sequences (Reyes-Caballero *et al.*, 2010). We demonstrate the predictive value of
137 this allosteric model by functionally characterizing “cavity” mutants of AdcR (Capdevila *et al.*,
138 2017a). Overall, our findings suggest that protein dynamics on a wide range of timescales
139 strongly impact AdcR function. This ensemble model of allosteric successfully reconciles the
140 distinct mechanisms proposed for other MarR family repressors and suggests a mechanism of
141 how evolution tunes dynamics to render distinct biological outputs (allosteric activation vs.
142 allosteric inhibition) on a rigorously conserved molecular scaffold.

143

144 **Results and Discussion**

145 **Solution structural differences between apo and Zn^{II} bound forms of AdcR**

146 Our crystal structure suggests that once AdcR is bound to both Zn^{II}, the α R- (α 4) reading
147 heads adopt a favorable orientation for DNA binding (Guerra *et al.*, 2011), a finding fully
148 compatible with structural studies of *L. lactis* ZitR (Zhu *et al.*, 2017c) (Fig. 1A). These
149 structural studies suggest a “pre-locked” model, where Zn^{II} binding to both sites 1 and 2,
150 concomitant with a H42 ligand atom switch, locks the AdcR homodimer into a DNA binding-
151 competent conformation. This model makes the prediction that the unligated AdcR can explore
152 conformations structurally incompatible with DNA binding, as shown previously for Zn^{II}₁ ZitR
153 (Zhu *et al.*, 2017c), thus requiring a significant degree of reorganization to bind with high

154 affinity to the DNA (Fig. 1B). Despite significant efforts, it has not yet been possible to obtain
155 the crystal structure of apo-AdcR, suggesting that the apo-repressor may be highly flexible in
156 solution (Guerra *et al.*, 2011, Sanson *et al.*, 2015). Thus, we employed SAXS as a means to
157 explore the apo-AdcR structure and elucidate the structural changes induced by Zn^{II} binding and
158 conformational switching within the AdcR homodimer.

159 We first examined the behavior of apo- and Zn^{II}-bound states. Both states show Guinier
160 plots indicative of monodispersity and similar radii of gyration (R_g). These data reveal that each
161 state is readily distinguished from the other in the raw scattering profiles (to $q=0.5 \text{ \AA}^{-1}$) as well as
162 in the PDDF plots ($p(r)$ *versus* r), with the experimental scattering curve of the Zn^{II} bound state
163 being consistent with one calculated from the Zn^{II}₂ AdcR crystal structure (Fig. 2A). Moreover,
164 a qualitative analysis of the PDDF plots suggests that apo-AdcR is less compact than the Zn^{II}-
165 bound state (Fig. S2). The molecular scattering envelopes calculated as bead models with the *ab*
166 *initio* program DAMMIF for apo-AdcR suggest that the differences between the apo and Zn^{II}
167 AdcR SAXS profiles can be explained on the basis of a reorientation of the winged helix-turn-
168 helix motif with respect to the dimerization domain, particularly in a distortion in the $\alpha 5$ helix
169 (Fig. 2B). In an effort to obtain higher resolution models, we reconstructed atomic models from
170 perturbations in the Zn-bound crystal structure that better fit the complete SAXS profiles
171 ($q<1.0$). The models obtained confirm that the Zn-bound structure in solution resembles the
172 crystallographic models of apo-ZitR and Zn^{II} AdcR (Guerra *et al.*, 2011, Zhu *et al.*, 2017c);
173 however, we note that the SAXS profile of the apo-AdcR differs significantly from the ZitR
174 crystal structure (Fig. S2E) which is likely related to the high flexibility of this state in solution.
175 Moreover, the resolution of SAXS based models cannot be used to obtain residue-specific
176 information about structural perturbations introduced by Zn^{II} binding (Fig. S2). Thus, we turned

177 to NMR-based techniques to provide both high resolution and site-specific information on this
178 highly dynamic system.

179 TROSY NMR on 100% deuterated AdcR and optimized buffer conditions for both states
180 (pH 5.5, 50 mM NaCl, 35 °C) enabled us to obtain complete backbone assignments for Zn^{II}-
181 AdcR and nearly complete for apo-AdcR (missing residues 21, 38-40 due to exchange
182 broadening, Fig. 3). The chemical shift perturbation maps (Fig. 3A-B) reveal that the largest
183 perturbations are found in the structural vicinity of the metal site region, *i.e.*, the α 1- α 2 loop
184 (residues 21-35), the remainder of the α 2 helix (residues 41-47), and the central region of the α 5
185 helix, which provides donor groups to both site 1 (H108, H112) and site 2 (E107) Zn^{II}. These
186 changes derive from changes in secondary structure, such as the extension of the α 1 helix and
187 partial unfolding of the α 2 helix (Fig. S3), as well as from proximity to the Zn^{II}.

188 The changes in carbon chemical shifts in the central region of the α 5 helix and the
189 presence of strong NOEs to water for these residues are consistent with a kink in this helix in the
190 apo-state (Fig. S3A-B), as is commonly found in other structurally characterized MarR
191 repressors in DNA-binding inactive conformations (Zhu *et al.*, 2017b, Duval *et al.*, 2013).
192 However, the kink is expected to be local and transient, since a TALOS+ analysis of chemical
193 shifts predicts that the α 5 helix remains the most probable secondary structure for all tripeptides
194 containing these residues in the apo-state (Shen *et al.*, 2009) (Fig. S3C). The backbone changes
195 in chemical shifts are accompanied by changes in the hydrophobic cores in the proximity of Zn^{II}
196 binding as reported by the stereospecific sidechain methyl group chemical shift perturbation
197 maps (Fig. 3B). Comparatively smaller perturbations extend to the α 1 helix and the C-terminal
198 region of the α 6 helix, DNA-binding α 4 helix (S74) and into the β -wing itself, consistent with a

199 significant change in quaternary within the AdcR homodimer upon binding of both allosteric
200 metal ions (Fig. 3A-B).

201 Overall, our NMR and SAXS data show that the main structural differences are localized
202 in the region immediately surrounding the Zn^{II} coordination sites, giving rise to a change in the
203 quaternary structure, while conserving the size and the overall secondary structure of the
204 molecule. In particular, our data point to a kink in the α 5 helix and a structural perturbation in
205 the α 1- α 2 loop, which could be inducing a reorientation of the winged helix-turn-helix motifs
206 relative to the dimerization domain.

207 In an effort to understand the functional consequences of the structural perturbations in
208 the α 1- α 2 loop, we compared the length of the loop that connects the dimerization domain with
209 the winged helical motif among AdcR and other members of the MarR family of known
210 structure. This structural comparison and an extensive multiple sequence alignment reveals that
211 only AdcR-like repressors harbor an α 1- α 2 loop larger than 10 residues (Fig. 3C). This loop
212 extension does not seem to originate from an insertion, but from a change in secondary structure
213 of the C-terminal region of the α 1 helix (Fig. 3C). Moreover, in the Zn^{II} state that loop appears
214 restricted by a hydrogen-bond network between the Zn^{II} binding site and the DNA binding
215 domain (Chakravorty *et al.*, 2013). The Zn^{II}-ZitR crystal structure similarly has an α 1- α 2 loop
216 that is restricted by metal coordination chemistry and other intermolecular contacts with the
217 dimerization and DNA binding domains, despite lacking an identifiable hydrogen-bond network
218 (Zhu *et al.*, 2017c). Overall, our analysis suggests that the flexibility of this loop prevents DNA-
219 binding, while the interactions formed in response to Zn^{II} coordination may be important in
220 allosteric activation of DNA binding. Such a dynamical model contrasts sharply with a rigid
221 body motion mechanism as previously suggested for other MarRs (Alekshun *et al.*, 2001, Chang

222 *et al.*, 2010, Dolan *et al.*, 2011, Saridakis *et al.*, 2008, Birukou *et al.*, 2014, Radhakrishnan *et al.*,
223 2014), thus motivating efforts to understand how conformational dynamics impacts biological
224 regulation by Zn^{II} in AdcR.

225

226 **Zn^{II}-induced changes in AdcR conformational plasticity along the backbone**

227 We therefore turned to an investigation of protein dynamics in AdcR. ¹⁵N R_1 , R_2 , and
228 steady-state heteronuclear ¹⁵N{¹H} NOEs provide information on internal mobility along the
229 backbone, as well as on the overall protein tumbling rate (Fig. 4A-D; Fig. S4). The R_1 and R_2
230 data reveal that Zn^{II}₂ AdcR tumbles predominantly as a single globular unit in solution (Fig. 4B;
231 Fig. S4) with a molecular correlation time (τ_c) of 18.7 ± 0.1 ns, very similar to the τ_c value
232 predicted for the dimer at 35 °C (18.9 ns in D₂O). The β-wing region tumbles independently
233 from the rest of the molecule (Fig. 4B). These data also reveal that the α1-α2 linker region that
234 donates the E24 ligand to Zn^{II} binding site 1 is ordered to an extent similar to the rest of the
235 molecule. In striking contrast, in apo-AdcR, the dimerization and DNA-binding domains have
236 significantly smaller τ_c values (10.9 ± 0.5 ns, Fig. 4A), close to that expected if these domains
237 tumble independently of one another in solution; in addition, the α1-α2 loop is highly dynamic
238 in the apo-state (see also Fig. S4). These findings are consistent with the SAXS data, which
239 show that apo-AdcR is less compact than the Zn^{II}₂ state. As in the Zn^{II}₂ state, the β-wing
240 tumbles independently of the rest of the molecule, revealing that a change in the flexibility or
241 orientation of the β-hairpin is likely not part of the allosteric mechanism, contrary to what has
242 been proposed for other MarRs on the basis of crystal structures alone (Liu *et al.*, 2017,
243 Deochand & Grove, 2017, Kim *et al.*, 2016). Overall, the ¹⁵N relaxation data for backbone
244 amides show that Zn^{II} binding leads to a reduction of mobility of the α1-α2 loop, which in turn,

245 decreases the dynamical independence the DNA-binding and dimerization domains, thereby
246 stabilizing a conformation that tumbles in solution as a single globular unit.

247 To further probe the reduction of flexibility upon Zn^{II} binding, we investigated sub-
248 nanosecond backbone mobility as reported by the steady-state heteronuclear ¹⁵N{¹H} NOEs
249 (Fig. 4C-D). These hNOE data confirm that the internal mobility of the apo-state on this
250 timescale mainly localizes to the α 1- α 2 loop and the central region of the α 5 helix, around E107
251 (Zn^{II} site 2 ligand) and H108 and H112 (Zn^{II} site 1 ligands). The short-timescale flexibility in
252 this region is significantly restricted upon Zn^{II} binding, but somewhat paradoxically leads to an
253 *increase* in sub-nanosecond backbone motion in the DNA-binding domain, particularly in the α 3
254 helix and the N-terminal region of the α 4 helix, which harbors the key DNA-binding
255 determinants (Fig. S1A) (Zhu *et al.*, 2017c). The quenching of sub-nanosecond mobility in the
256 α 1- α 2 loop by Zn^{II} is accompanied by a corresponding increase in mobility on the μ s-ms (slow)
257 timescale in this region (Fig. 4F). In addition, the slow timescale backbone dynamics show a
258 restriction of a conformational sampling in a band across the middle of the dimerization domain,
259 including the upper region of the α 5 helix, the N-terminus of α 1, and the C-terminus of α 6 (Fig.
260 4E-F). These slow motions in the apo-state likely report on a global breathing mode of the
261 homodimer reflective of the conformational ensemble, which is substantially restricted upon Zn^{II}
262 binding.

263 These large differences in structure and dynamics between the apo and Zn^{II}₂ AdcRs
264 suggest an allosteric mechanism that relies on a redistribution of internal mobility in both fast-
265 and slow timescale regimes, rather than one described by a rigid body motion. This mobility
266 redistribution restricts the flexibility of the ligand binding site from the sub-nanosecond
267 timescale in the apo-form to the millisecond timescale in the Zn^{II}₂ state (Fig. 4C,F). This

268 restriction links the motion of the two functional domains (Fig. 4A-B) and locks AdcR in a
269 triangular shape compatible with DNA binding. On the other hand, Zn^{II} enhances the internal
270 flexibility in the DNA binding domain (Fig. 4C-D), which other studies show plays a role in
271 sequence recognition and high affinity binding, particularly on the side chains (Capdevila *et al.*,
272 2017a, Kalodimos *et al.*, 2004, Anderson *et al.*, 2013).

273

274 **Zn^{II}-induced perturbations of side chain conformational disorder in AdcR**

275 Unlike the backbone, perturbations in side chain flexibility in the sub-nanosecond
276 timescale are capable of reporting on the underlying thermodynamics of Zn^{II} binding and the role
277 of conformational entropy (ΔS_{conf}) in the allosteric mechanism. These perturbations potentially
278 pinpoint residues with functional roles, *i.e.*, allosteric hotspots (Capdevila *et al.*, 2017a), with the
279 change in the methyl group order parameter (ΔS_{axis}^2) upon ligand binding employed as a
280 dynamical proxy (Capdevila *et al.*, 2017a, Caro *et al.*, 2017). Thus, if the motional redistribution
281 observed in the backbone upon Zn^{II} binding is accompanied by changes in the dynamics on the
282 side chains, particularly those in the DNA binding regions, these fast internal dynamics could
283 affect the entropy of the metal binding and play a major role in the allosteric mechanism. To test
284 these ideas, we first measured the axial order parameter, S_{axis}^2 , for all 82 methyl groups,
285 comparing the apo- and Zn-bound states of AdcR (Fig. 5A, Fig. S5). These dynamics changes
286 are overall consistent with the stiffening observed along protein backbone, *e.g.*, in the $\alpha 1$ - $\alpha 2$
287 loop; L26, in particular, is strongly impacted, changing motional regimes, $|\Delta S_{\text{axis}}^2| > 0.2$)
288 (Frederick *et al.*, 2007). This stiffening prevails all over the molecule, leading to a small net
289 decrease in conformational entropy upon Zn^{II} coordination ($-T\Delta S_{\text{conf}} = 3.4 \pm 0.4 \text{ kcal mol}^{-1}$) (Fig.
290 5A). However, as has been previously shown for other transcriptional regulators (Capdevila *et*
291 *al.*, 2017a, Tzeng & Kalodimos, 2012), the binding of the allosteric ligand Zn^{II} actually leads to a

292 redistribution of sidechain mobility throughout the entire molecular scaffold. Interestingly, most
293 of the methyl groups that change motional regimes are located in the DNA binding domain (Fig.
294 S7). In particular, the side chain flexibility of many residues in the α 3 helix *increases*, including
295 L47, L57, L61, while a small hydrophobic core in the C-terminus of the α 4 helix stiffens
296 significantly, *e.g.*, L81, V34. These changes are accompanied by perturbations in the dynamics at
297 the dimer interface, *i.e.*, L4, I16, V14, in both motional regimes as reported by ΔS^2_{axis} and ΔR_{ex}
298 (in the μ s-ms timescale), the latter derived from relaxation dispersion experiments (Table S2;
299 Fig. S5C).

300

301 **On-pathway and off-pathway allosterically impaired mutants of AdcR**

302 Our previous work (Capdevila *et al.*, 2017a) makes the prediction that “dynamically
303 active” sidechains (methyl groups with $|\Delta S^2_{\text{axis}}| \geq 0.2$ upon Zn^{II} binding) (see Fig. 5) are crucial for
304 allosteric activation of DNA binding by Zn^{II} . To test this prediction, we prepared and
305 characterized several mutant AdcRs in an effort to disrupt allosteric activation of DNA binding,
306 while maintaining the structure of the dimer and high affinity Zn^{II} binding. Since it was not clear
307 *a priori* how mutations that perturb mobility distributions in one timescale or the other (sub-ns or
308 μ s-ms) would impact function, we focused on two kinds of substitution mutants: cavity mutants
309 of dynamically “active” methyl-bearing side chains positioned in either the DNA binding or the
310 dimerization subdomains (Fig. 6A, B) (Capdevila *et al.*, 2017a), and substitutions in the
311 hydrogen-bonding pathway in the Zn-state that may contribute to the rigidity of the α 1- α 2 loop
312 in Zn^{II}_2 -AdcR (Fig. 6A) (Chakravorty *et al.*, 2013). We measured DNA binding affinities of the
313 apo and zinc-saturated Zn^{II}_2 -states, and calculated the allosteric coupling free energy, ΔG_c , from
314 $\Delta G_c = -RT\ln(K_{\text{Zn,DNA}}/K_{\text{apo,DNA}})$ (Giedroc & Arunkumar, 2007) (Fig. 6C and Table S2). All

315 mutants are homodimers by size-exclusion chromatography (Fig. S9) and all bind the first
316 equivalent of Zn^{II} tightly as wild-type AdcR (Fig. S10, Table S3).

317 *DNA-binding domain mutants.* The redistribution fast time scale side-chain dynamics in
318 the DNA binding domain is delocalized throughout the different secondary structure motifs.

319 Thus, we prepared several cavity mutants of methyl-bearing residues in the α 3 (L57, L61), α 4
320 (L81) and α 5 (I104) helices, as well as two residues in the α 1- α 2 loop in close proximity to the
321 N-terminus of α 2, V34 and L36. I104 is the most distal from the bound DNA in the Zn^{II}₂ ZitR-
322 DNA complex (Zhu *et al.*, 2017c), and is not dynamically active in AdcR ($|\Delta S^2_{\text{axis}}| < 0.1$;
323 $\Delta R_{\text{ex}} < 1.0$); thus, the I104A mutant is predicted to function as a control substitution. V34 and L36
324 are dynamically active on both timescales, which is not surprising since the α 1- α 2 loop folds
325 upon Zn^{II} binding to AdcR (*vide supra*) (Zhu *et al.*, 2017c). In contrast, L57, L61 and L81 are
326 characterized by significant perturbations in ΔS^2_{axis} only ($|\Delta S^2_{\text{axis}}| \geq 0.2$), with L81 stiffening and
327 L57 and L61 methyls in the α 3 helix becoming significantly more dynamic upon Zn^{II} binding
328 (Fig. 5A, Table S2).

329 As expected, I104A AdcR is characterized by DNA binding affinities in the apo- and Zn-
330 states just \approx 2-fold lower than wild-type AdcR, returning a ΔG_c that is not statistically different
331 from wild-type AdcR (Fig. 6C). Functional characterization of all other cavity mutants in the
332 DNA binding domain results in a \approx 5-10-fold decrease or greater (L57V AdcR; Table S2) in the
333 DNA binding affinity of the apo-state (Fig. 6C), with Zn^{II} binding inducing markedly variable
334 degrees of allosteric activation (Fig. 6C). L36A, closest to the α 2 N-terminus, is most like wild-
335 type AdcR, while V34A AdcR is severely crippled in allostery, with $K_{\text{Zn,DNA}}$ some 200-fold
336 lower than wild-type AdcR, and $\Delta G_c \approx$ 2-fold lower, from -4.0 to -2.2 kcal mol⁻¹. L81V and
337 L61A AdcRs are comparably perturbed, and L57M AdcR even more so ($\Delta G_c \approx -2.0$ kcal mol⁻¹).

338 We emphasize that these methyl-bearing side chains targeted for substitution are $\geq 95\%$ buried
339 and none are expected to be in direct contact with the DNA (Fig. 6B, Table SI). These data
340 provide strong support for the idea that those methyl-bearing side chains in the DNA-binding
341 domain that exhibit large changes in conformational entropy (as measured by ΔS^2_{axis}) make
342 significant contributions to both DNA binding and allosteric activation by Zn^{II} . This result
343 highlights the contribution that dynamical redistribution within the DNA-binding domain makes
344 for AdcR function, as has been observed in other transcriptional regulators (Tzeng & Kalodimos,
345 2012; Capdevila *et al.*, 2017a).

346 *Hydrogen-bonding mutants.* A hydrogen-bonding pathway in AdcR (Chakravorty *et al.*,
347 2013) has previously been proposed to transmit the Zn^{II}_2 binding signal to the DNA binding
348 domain. In this pathway, the O ϵ 1 atom from the Zn^{II} ligand E24 accepts a hydrogen bond from
349 the carboxamide side chain of N38. N38 is the +1 residue of the α 2 helix, which is then
350 connected to the α 4 helix via a hydrogen bond between the Q40 and S74 side chains; further,
351 Q40 accepts a hydrogen bond from the γ -OH of T37 as part of a non-canonical helix N-capping
352 interaction (Guerra *et al.*, 2011) (Fig. 6A). We expect that regardless of the impact that these
353 interactions have on the overall energetics of Zn^{II} binding, they are important in the restriction of
354 fast-time scale dynamics in the α 1- α 2 loop. We therefore targeted residues E24 (Zn-ligand and
355 H-bound acceptor), N38 and Q40, by characterizing two single mutants, E24D and N38A, and
356 the double mutant, N38A/Q40A AdcR. Although all three mutants undergo allosteric switching
357 as revealed by ^1H - ^{15}N TROSY spectra (Fig. S11), as with all other DNA-binding domain
358 mutants, all three exhibit \approx 5-10-fold decreases in apo-state DNA-binding affinity (Fig. 6C; Table
359 S2). While the single mutant N38A binds Zn^{II} to give ΔG_c of $\approx -3.5 \text{ kcal mol}^{-1}$, quite similar to
360 that of wild-type AdcR, in marked contrast, N38A/Q40A AdcR is functionally perturbed,
361 characterized by a ΔG_c of $\approx -1.9 \text{ kcal mol}^{-1}$ and is E24D AdcR that target a Zn^{II} binding residue

362 (Fig. 6C). These perturbations provide additional evidence that this hydrogen-bonding pathway
363 may contribute to the motional restriction of the α 1- α 2 loop, jointly with a redistribution of
364 internal dynamics in the DNA binding domain. This effect can be perturbed directly by mutation
365 of “dynamically active” sidechains (L81V, L61V, L57M) or by significantly impacting the
366 interactions that restrict the loop (N38A/Q40A).

367 *Dimerization domain mutants.* To test the functional role of the dimerization domain in
368 dynamical changes, we targeted three methyl-bearing residues in this domain, including L4 and
369 I16 on opposite ends of the α 1 helix and V142, near the C-terminus of the α 6 helix (Fig. 6B).
370 L16 is closest to the intervening minor groove of the DNA operator, while V142 and L4 are
371 increasingly distant from the DNA. These residues are primarily active in slow timescale
372 dynamics, with Zn^{II} -binding quenching side chain mobility on the μ s-ms timescale, *i.e.*, global
373 motions, but relatively smaller changes in ΔS_{axis}^2 (Fig. 5B; Table S2). Cavity mutants of these
374 residues (I16A, L4A and V142A) bind DNA in the apo-state with wild-type like affinities, but
375 each is allosterically strongly perturbed, with only \approx 10-20-fold allosteric activation by Zn^{II} ,
376 giving ΔG_c values of -1.4 to -1.8 kcal mol $^{-1}$.

377 These findings suggest that Zn^{II} -dependent quenching of global motions far from the
378 DNA binding domain play a significant role in allostery in this system. Our characterization of
379 allosterically compromised mutants that affect site-specific conformational entropy (L81V,
380 L61V, L57M) and conformational exchange (V34A, L4A, I16A) provides evidence for two
381 classes of functional dynamics in AdcR that comprise different regions of the molecule,
382 operating on different timescales (from sub-nanoseconds to milliseconds). Thus, we propose that
383 a Zn^{II} -dependent redistribution of internal dynamics quenches global, slow motions in the dimer,
384 yet enhances local dynamical disorder in the DNA binding domain, which can ultimately be
385 harnessed to maximize contacts at the protein-DNA interface.

386 Conclusions

387 Members of the multiple antibiotic resistance repressor (MarR) family of proteins
388 comprise at least 12,000 members (Capdevila *et al.*, 2017b), and many have been subjected to
389 significant structural inquiry since the original discovery of the *E. coli* *mar* operon and
390 characterization of *E. coli* MarR some 25 years ago (Cohen *et al.*, 1993, Seoane & Levy, 1995).
391 The crystallographic structure of this prototypical *E. coli* MarR appeared a number of years later
392 (Alekshun *et al.*, 2001) and has inspired considerable efforts to understand the inducer specificity
393 and mechanisms of transcriptional regulation in *E. coli* MarR (Hao *et al.*, 2014) and other MarR
394 family repressors (Grove, 2013), which collectively respond to a wide range of stimuli,
395 including small molecules, metal ions, antibiotic and oxidative stress (Deochand & Grove,
396 2017). We have examined the wealth of the crystallographic data available from 137 MarR
397 family repressor structures solved in a variety of functional states, including DNA-binding
398 competent, DNA-binding incompetent and DNA-bound states (Fig. 1). This analysis of the
399 crystal structures suggests that conformational selection induced by ligand binding or thiol
400 oxidation must be operative in a significant number of these repressor systems. Here, we present
401 the first site-specific dynamics analysis of any MarR family repressor in solution, and establish
402 that conformational dynamics on a range of timescales is a central feature of Zn^{II}-dependent
403 allosteric activation of DNA operator binding by the zinc uptake regulator, *S. pneumoniae* AdcR
404 (Reyes-Caballero *et al.*, 2010) and closely related repressors (Zhu *et al.*, 2017c).

405 We explored dynamics in the sub-nanosecond and μs-ms timescales with residue-specific
406 resolution, both along the backbone, as measured by N-H bond vectors, and in the methyl groups
407 of the methyl-bearing side chains of Ala, Met, Val, Leu and Ile. These measurements, coupled
408 with small angle x-ray scattering measurements of both conformational states, lead to a
409 consistent picture of allosteric activation by Zn^{II} in AdcR. The apo-state conformational

410 ensemble is far broader than the Zn^{II}₂ state, and features dynamical uncoupling of the core DNA-
411 binding and dimerization domains, facilitated by rapid, low amplitude motions in the α 1- α 2 loop
412 and the α 5 helix in the immediate vicinity of the Zn^{II} coordinating residues. This motion is
413 superimposed on a much slower, larger amplitude mobility across the dimerization domain, far
414 from the DNA interface, affecting both backbone amide and side chain methyl groups (Fig. 4-5).
415 Zn^{II} binding substantially quenches both the low amplitude internal motions and global, larger
416 amplitude movements, while driving a striking redistribution of these dynamics into the DNA-
417 binding domain.

418 As we observed previously for another Zn^{II} metalloregulatory protein, Zn^{II} binding
419 induces a net global conformational stiffening, superimposed on pockets of increased dynamical
420 disorder, particularly in the α 3- α 4 region of the DNA binding domain (Fig. 5A). It is interesting
421 to note that the structures of Zn^{II}₂-bound AdcR and DNA-bound Zn^{II}₂ ZitR differ most strongly
422 in the α 3- α 4 region (Fig. 6B), suggesting that internal dynamics in this region may be
423 functionally important in enhancing DNA binding affinity. To test the functional importance of
424 fast-time scale motions in the DNA binding domain, we exploited the side chain dynamics
425 results (Fig. 5) (Capdevila *et al.*, 2017a) to design cavity substitutions of dynamically active
426 residues (Fig. 6). We generally find that cavity substitutions in the DNA binding domain are
427 strongly deleterious for residues that are dynamically active in the fast timescale ($|\Delta S^2_{\text{axis}}| > 0.2$),
428 *i.e.* L81, L61, L57. These findings confirm a functional role of these changes in dynamics
429 (Capdevila *et al.*, 2017a) and suggest that Zn^{II}₂-bound AdcR has an optimal distribution of
430 internal dynamics that if perturbed, leads to weakened DNA binding.

431 Crystallographic studies suggest that DNA binding in MarR repressors is optimized by
432 precisely tuning interactions with the DNA operator sequence, resulting in a favorable ΔH of

433 binding (Hong *et al.*, 2005, Dolan *et al.*, 2011, Quade *et al.*, 2012, Birukou *et al.*, 2014, Zhu *et*
434 *al.*, 2017a, Gao *et al.*, 2017, Otani *et al.*, 2016) with the functional consequences of ligand
435 binding known to vary widely among individual MarRs (Deochand & Grove, 2017). We
436 propose here, based on this and previous work, that tighter DNA binding can be achieved by
437 optimization of side-chain dynamics that give rise to a more favorable conformational entropy
438 term (ΔS_{conf}) and the functional consequences of ligand binding can be predicted based on the
439 protein internal motions. We show here that single point mutations in AdcR, sufficient to impact
440 internal motions, result in destabilization of the ternary complex. We showed previously that
441 ligand binding can inhibit formation of the DNA complex by restricting the coupled fast motions
442 and concerted slower motions that contribute to a favorable conformational entropy of DNA
443 binding (Capdevila *et al.*, 2017a). This can potentially be the case also for introduction of
444 dynamic elements, *i.e.*, loops or disordered regions (Pabis *et al.*, 2018, Campbell *et al.*, 2016).
445 Thus, in the context of evolution of the MarR repressors, we propose that two allosteric modes,
446 activation and inhibition, may have evolved by tuning the conformational entropy contribution to
447 DNA binding (Fig. 7).

448 Allosteric inhibition could have arisen by evolution of a ligand binding pocket where
449 inducer recognition disrupts internal dynamics and increases the conformational entropic cost of
450 binding to DNA, as we have previously shown for an ArsR family protein (Capdevila *et al.*,
451 2017a). Although this hypothesis has not been tested experimentally on any MarR, molecular
452 dynamics simulations show that DNA binding-impaired mutants of MexR differ from the wild-
453 type repressor in the nature of the dynamical connection between the dimerization and DNA
454 binding domains (Anandapadamanaban *et al.*, 2016). This dynamical connectivity is in fact,
455 exploited by the binding the ArmR peptide, leading to DNA dissociation (Anandapadamanaban
456 *et al.*, 2016, Wilke *et al.*, 2008). We propose that conformational entropy can contribute to other

457 mechanisms of allosteric inhibition to yield a repressor that binds tightly to the operator sequence
458 and yet has the ability to readily evolve new inducer specificities.

459 On the other hand, allosteric activation could have evolved by perturbing internal
460 dynamics on the apo-protein and increasing the conformational entropic cost of DNA binding.
461 This perturbation could arise by the introduction of loops or disordered regions in the apo-protein
462 that could be compensated by a ligand binding event that restores the internal dynamics to yield a
463 more favorable entropy contribution to DNA binding (Fig. 7). Similarly, it has been shown that
464 another well-studied, allosterically activated, bacterial regulator, catabolite activator protein
465 (CAP) (Tzeng & Kalodimos, 2013, Tzeng & Kalodimos, 2012) is able to harness conformational
466 entropy to increase DNA binding affinity upon ligand binding. In the case of MarRs, the far
467 longer α 1- α 2 linker in AdcRs (Fig. 3) may have been an important intermediate determinant in
468 the evolution of allostery in AdcR, given the key role this loop plays in dynamical uncoupling of
469 the dimerization and DNA-binding domains in the ligand-free state (Fig. 7).

470 This model makes the prediction that if conformational entropy can be harnessed to bind
471 DNA with high affinity, perturbations introduced by ligand binding or subtle change in protein
472 sequence that conserve the molecular scaffold can easily lead to inactivation of DNA binding
473 (Fig. 7). It is interesting to note that mutations that lead to inactivation are not necessarily part of
474 a physical pathway with the DNA binding site (Clarke *et al.*, 2016), since they only need to
475 affect dynamical properties that are likely delocalized in an extended network. Notably, single
476 point mutants in the dimerization domain of various MarR family repressors have been shown to
477 modulate allostery and DNA binding (Anandapadamanaban *et al.*, 2016, Deochand *et al.*, 2016,
478 Liguori *et al.*, 2016, Duval *et al.*, 2013, Alekshun & Levy, 1999, Andresen *et al.*, 2010). In the
479 case of AdcR, structural perturbations induced by Zn^{II} binding are essentially confined to the Zn^{II}
480 binding pocket, *i.e.*, the α 1- α 2 loop and the α 5 helix proximal to the Zn^{II} donor ligands (Fig. 3).

481 In striking contrast, dynamical perturbations extend all over the molecule, and feature many
482 residues that are far from either ligand binding site, and are dynamically active on the sub-
483 nanosecond and/or μ s-ms timescales (Figs. 4-5). Thus, the conformational entropy contribution
484 being inherently delocalized and easily perturbed can enable rapid optimization of new
485 inactivation mechanisms that would allow new biological functionalities to arise (Fig 7).
486 Moreover, we suggest that changes in the site-specific dynamics, derived from differences in the
487 amino acid sequence, could evolve allosteric activation from allosteric inhibition in the context
488 of the same overall molecular scaffold. These findings inspire efforts to explore the evolution of
489 allostery in this remarkable family of transcriptional repressors, by exploiting an allosterically
490 crippled AdcR (see Fig. 6) to re-evolve functional allostery on this system.

491

492 **Materials and Methods**

493 **AdcR mutant plasmid production**

494 An overexpression plasmid for *S. pneumoniae* AdcR in a pET3a vector was obtained as
495 previously described and was used as a template for the production of all mutant plasmids
496 (Reyes-Caballero *et al.*, 2010). Mutant AdcR plasmids were constructed by PCR-based site-
497 directed mutagenesis, and verified using DNA sequencing.

498

499 **Protein production and purification**

500 AdcR plasmids were transformed into either *E. coli* BL21(DE3) pLysS or Rosetta cells. *E. coli*
501 cultures were either grown in LB media or M9 minimal media supplemented with $^{15}\text{NH}_4\text{Cl}$ as the
502 sole nitrogen source with simple $^1\text{H}, ^{15}\text{N}$ HSQC spectroscopy to assess the structural integrity of
503 selected mutant proteins. Protein samples for backbone and methyl group assignments of AdcR

504 were isotopically labeled using published procedures as described in our previous work
505 (Capdevila *et al.*, 2017a, Arunkumar *et al.*, 2007), with all isotopes for NMR experiments
506 purchased from Cambridge Isotope Laboratories. Protein expression and purification were
507 carried out essentially as previously described (Reyes-Caballero *et al.*, 2010). All proteins were
508 confirmed to have <0.05 molar equivalents of Zn(II) as measured by atomic absorption
509 spectroscopy and were dimeric by gel filtration chromatography. The AdcR protein
510 concentration was measured using the estimated molar extinction coefficient at 280 nm of 2980
511 $M^{-1} cm^{-1}$.

512

513 **Small angle x-ray scattering experiments**

514 Small angle and wide angle x-ray scattering data of the apo and Zn^{II}_2 states of AdcR was
515 collected at three different protein concentrations (5 mg/mL, 2.5 mg/mL and 1.25 mg/mL) in
516 buffer 25 mM MES pH 5.5, 400 mM NaCl, 2 mM EDTA/10 μ M ZnCl₂, 2 mM TCEP at sector
517 12ID-B at the Advanced Photo Source (APS) at Argonne National Laboratory. For each protein
518 concentration and matching background buffer, 30 images were collected and averaged using
519 NCI-SAXS program package. The scattering profile at each concentration was manually
520 adjusted with the scale factor to remove the effect of concentration prior to subtraction of the
521 scattering profile of the buffer. Scattering profiles of each protein concentration were then
522 merged for further analysis. The GUINIER region was plotted with $\ln(I(q))$ vs q^2 to check for
523 monodispersity of the sample and to obtain I_0 and the radius of gyration (R_g) within the range of
524 $q_{max} * R_g < 1.3$. The R_g values obtained for apo-AdcR and Zn(II)-bound-AdcR are $25.5 \pm 0.9 \text{ \AA}$ and
525 $23.7 \pm 1.1 \text{ \AA}$, respectively. The scattering profiles of each AdcR conformational state was then
526 normalized with I_0 . The compaction of each states of AdcR was examined using the Kratky plot
527 for $q < 0.3 \text{ \AA}^{-1}$. Scattering profiles for apo and Zn^{II}_2 states of AdcR were then Fourier-transformed

528 using GNOM of the ATSAS package to obtain the normalized pair-wise distance distribution
529 graph (PDDF).

530 *Ab initio* modeling was performed using the program DAMMIF in a slow mode (Franke
531 & Svergun, 2009). For each conformational state of AdcR, 10 models were obtained. These
532 models were compared, aligned and averaged using the DAMSEL, DAMSUP, DAMAVER,
533 DAMFILT, respectively, as described in the ATSAS package ([http://www.embl-
534 hamburg.de/bioSAXS](http://www.embl-hamburg.de/bioSAXS)). Normalized spatial discrepancy (NSD) between each pair of the models
535 was computed. The model with the lowest NSD value was selected as the reference against
536 which the other models were superimposed. Outliner models (2 models) with an NSD above
537 mean + 2*standard deviation of NSD were removed before averaging. For refinement, the
538 averaged envelope of the first run was used as search volume for the second round of modeling.
539 Modeling of the envelope of apo-AdcR was restrained by enforcing P_2 rotational symmetry
540 while that Zn^{II}_2 AdcR was restrained using compact, hallow and no-penalty constraints.
541 Scattering profiles of crystal structures were calculated using the fast x-ray scattering (FOXS)
542 webserver (<https://modbase.compbio.ucsf.edu/foxs/>) (Schneidman-Duhovny *et al.*, 2010).

543

544 **Mag-fura-2 competition assays**

545 All mag-fura-2 competition experiments were performed on an ISS PC1 spectrofluorometer in
546 operating steady-state mode or a HP8453 UV-Vis spectrophotometer as described in our
547 previous work (Capdevila *et al.*, 2017a, Campanello *et al.*, 2013) using the following solution
548 conditions: 10 mM Hepes, pH 7.2, 400 mM NaCl that was chelex treated to remove
549 contaminating metals. 10 μ M protein concentration was used for all and MF2 concentration
550 ranged from 13-16 μ M. These data were fit using a competitive binding model with DynaFit
551 (Kuzmic, 1996) to determine zinc binding affinities for wild-type and each mutant AdcR using a

552 four-site-nondissociable homodimer binding model, as previously described (Reyes-Caballero *et*
553 *al.*, 2010) with $K_{Zn} = 4.9 \times 10^6 \text{ M}^{-1}$ for mag-fura-2 fixed in these fits. K_1 and K_2 correspond to
554 filling the two high affinity sites (site 1), and only a lower limits ($\geq 10^9 \text{ M}^{-1}$) could be obtained for
555 these sites; K_3 and K_4 were allowed to vary in the fit, and are reported in Table S3. Experiments
556 were conducted 3 times for each AdcR variant. Errors of the binding constant parameters were
557 estimated from global fits.

558

559 **NMR spectroscopy**

560 NMR spectra were acquired on a Varian VNMRS 600 or 800 MHz spectrometer, each equipped
561 with a cryogenic probe, at the Indiana University METACyt Biomolecular NMR laboratory.

562 The two-dimensional spectra were processed using NMRPipe (Delaglio *et al.*, 1995). The three-
563 dimensional spectra were acquired using Poisson-gap non-uniform sampling and reconstructed
564 using hmsIST (Hyberts *et al.*, 2012) and analyzed using SPARKY (Goddard & Kneller) or
565 CARA (<http://cara.nmr.ch>). Typical solution conditions were $\sim 500 \mu\text{M}$ protein (protomer), 25
566 mM MES pH 5.5, 50 mM NaCl, 1 mM TCEP, 0.02% (w/v) NaN_3 , and 10 % D_2O . Some spectra
567 were recorded at pH 6.0 as indicated. Our previous NMR studies of AdcR (Guerra *et al.*, 2011,
568 Guerra & Giedroc, 2014) were carried out with samples containing $\approx 70\%$ random fractional
569 deuteration, pH 6.0, 50 mM NaCl, 35 °C; under those conditions, the backbone amides of
570 residues 21-26 in the $\alpha 1$ - $\alpha 2$ loop and harboring zinc ligand E24 as well as the N-terminal region
571 of the $\alpha 2$ helix (residues 37-40) exhibited significant conformational exchange broadening in the
572 apo-state and could not be assigned (Guerra *et al.*, 2011). In this work, we acquired
573 comprehensive ^1H - ^{15}N TROSY-edited NMR data sets at 600 and 800 MHz for a 100%
574 deuterated AdcR sample in both apo- and Zn_2 -bound states at pH 5.5, 50 mM NaCl, 35° C.
575 Under these conditions, only four backbone amides residues in the apo-state were broadened

576 beyond detection (residues 21, 38-40); all were visible and therefore assignable in the Zn^{II}_2 state.
577 Thus, the N-terminus of the α 2 helix, including N38 and Q40 are clearly exchange broadened in
578 the apo-state. Sidechains were assigned following published procedures as described in our
579 previous work (Capdevila *et al.*, 2017a, Arunkumar *et al.*, 2007). The Leu and Val methyl
580 resonances were distinguished using through-bond information such as HMCMCBCA or
581 HMCM[CG]CBCA experiments (Tugarinov & Kay, 2003) which correlate the Leu or Val
582 methyl resonances with other side chain carbon resonances. All apo-protein samples contained 1
583 mM EDTA. All Zn^{II}_2 samples contained 2 monomer mol equiv of Zn(II). Chemical shifts were
584 referenced to 2,2-dimethyl-2-silapentane-5-sulfonic acid (DSS; Sigma) (Wishart & Sykes, 1994).

585 S^2_{axis} of the Ile δ 1, Leu δ 1/ δ 2, Val γ 1/ γ 2, Ala β , and Met ε methyl groups in apo
586 and Zn(II) $_2$ states were determined using ^1H spin-based relaxation experiments at 600
587 MHz at 35.0 °C (Tugarinov *et al.*, 2007). S^2_{axis} values, cross-correlated relaxation rates,
588 η , between pairs of ^1H - ^1H vectors in $^{13}\text{CH}_3$ methyl groups were measured using Eq. 2

$$589 \eta = \frac{R_{2,H}^F - R_{2,H}^S}{2} \approx \frac{9}{10} \left(\frac{\mu_0}{4\pi} \right)^2 [P_2(\cos\theta_{\text{axis},HH})]^2 \frac{S_{\text{axis}}^2 \gamma_H^4 \hbar^2 \tau_c}{r_{HH}^6} \quad (2)$$

590 where τ_c is the tumbling time of the protein; $R_{2,H}^F$ and $R_{2,H}^S$ are the fast and slow relaxing
591 magnetization, respectively; γ_H is the gyromagnetic ratio of the proton; and r_{HH} is the
592 distance between pairs of methyl protons.

593 In order to obtain an approximation of the differences in fast and slow relaxation rates (2η),
594 we measured the time-dependence of the cross peak intensities in a correlated pair of single and
595 double quantum (2Q) experiments (Tugarinov *et al.*, 2007). Using various delay time, T , values
596 (3, 5, 8, 12, 17, 22, and 27 ms, recorded in an interleaved manner), the rates of η were obtained by
597 fitting ratios of peak intensities measured in pairs of experiments (I_a and I_b , spin-forbidden and
598 spin-allowed, respectively) with Eq. 3:

599
$$\frac{I_a}{I_b} = \frac{-0.5\eta \tanh(\sqrt{\eta^2 + \delta^2}T)}{\sqrt{\eta^2 + \delta^2} - \delta \tanh(\sqrt{\eta^2 + \delta^2}T)} \quad (3)$$

600 where T is the variable delay time, δ is a parameter that is related to the ^1H spin density around the
601 methyl group, and I_a and I_b are the time dependencies of differences and sums, respectively, of
602 magnetization derived from methyl ^1H single-quantum transitions, as described (Tugarinov *et al.*,
603 2007). Peak heights and spectral noise were measured in Sparky (Lee *et al.*, 2015). A python script
604 was used to fit the peak height ratios to η values and to determine S_{axis}^2 values in the apo- or Zn-
605 bound states, as described previously (Tugarinov & Kay, 2004, Tugarinov *et al.*, 2007, Capdevila
606 *et al.*, 2017a). τ_c was obtained from Monte Carlo simulations with tensor2 software (Dosset *et al.*,
607 2000), using T_1 , T_2 , and heteronuclear NOE (hNOE) recorded at 35 °C at 800 MHz, in 10% D_2O .
608 To enable a direct comparison of each AdcR allosteric state while overcoming the difficulty of
609 determining an isotropic τ_c from tensor2 for apo-AdcR (which harbors dynamically independent
610 domains), the measured τ_c for each state was obtained by adjusting S_{axis}^2 of alanine methyls to 0.85
611 since these methyl groups are generally motionally restricted in proteins (Igumenova *et al.*, 2006).
612 For apo- and Zn^{II}_2 AdcRs, the τ_c obtained in this way is 18.9 ± 0.1 ns and 20.7 ± 0.1 ns respectively.

613 Relaxation dispersion measurements were acquired using a TROSY adaptation of
614 ^{15}N and a ^1H - ^{13}C HMQC-based Carr–Purcell–Meiboom–Gill (CPMG) pulse sequence for
615 amides from the backbone (Tollinger *et al.*, 2001) and methyl groups from the sidechains
616 (Korzhnev *et al.*, 2004), respectively. Experiments were performed at 35 °C at 600 and
617 800 MHz ^1H frequencies using constant time interval $T=40$ ms with CPMG field
618 strengths (v_{CPMG}) of 50, 100, 150, 200, 250, 300, 350, 400, 450, 500, 600, 700, 850, and
619 1,000 Hz. Data were fitted to the two-site fast exchange limit equation, as discussed
620 previously (Capdevila *et al.*, 2017a). These experiments were performed on duplicate at
621 the two field strengths.

622

623 **DNA binding experiments and determination of allosteric coupling free energies (ΔG_c).**

624 For all DNA binding experiments a 28 bp double stranded DNA was obtained as previously

625 described (Reyes-Caballero *et al.*, 2010) with the following sequence of the AdcO: 5'-

626 TGATATAATTAACTGGTAAA CAAA ATGT[F]-3'. Apo AdcR binding experiments were

627 conducted in solution conditions of 10 mM HEPES, pH 7.0, 0.23 M NaCl, 1 mM TCEP

628 (chelexed), 10 nM DNA, 25.0 °C with 2.0 mM EDTA (for apo-AdcR) or 20 μ M ZnCl₂ (for Zn^{II})

629 AdcR) added to these reactions. Anisotropy experiments were performed on an ISS PC1

630 spectrofluorometer in steady-state mode with Glan-Thompson polarizers in the L-format. The

631 excitation wavelength was set at 494 nm with a 1 mm slit and the total emission intensity

632 collected through a 515 nm filter. For Zn(II)-bound-AdcR DNA-binding experiments, the data

633 were fit with DynaFit (Kuzmic, 1996) using a non-dissociable dimer 1:1 dimer:DNA binding

634 model ($K_{dim} = 10^{12} \text{ M}^{-1}$). For Zn(II)-bound experiments, the initial anisotropy (r_0) was fixed to

635 the measured value for the free DNA, with the anisotropy response of the saturated protein:DNA

636 complex ($r_{complex}$) optimized during a nonlinear least squares fit using DynaFit (Kuzmic, 1996).

637 Apo binding data were fit in the same manner, except $r_{complex}$ was fixed to reflect the anisotropy

638 change ($r_{complex} - r_0$) observed for wild-type AdcR in the presence of zinc. The errors on $K_{apo,DNA}$

639 and $K_{Zn,DNA}$ reflect the standard deviation of 3 independent titrations (Table S2). The coupling

640 free energies were calculated using the following equation: $\Delta G_c = -RT\ln(K_{Zn,DNA} / K_{apo,DNA})$

641 (Giedroc & Arunkumar, 2007). Negative values of ΔG_c were observed since AdcR is a positive

642 allosteric activator in the presence of Zn^{II} ($K_{apo,DNA} < K_{Zn,DNA}$).

643

644 **Acknowledgements**

645 We gratefully acknowledge support of this work by the NIH (R35 GM118157 to D. P. G.).
646 NMR instrumentation in the METACyt Biomolecular NMR Laboratory at Indiana University
647 was generously supported by a grant from the Lilly Endowment. D.A.C. acknowledges support
648 from the Pew Latin American Fellows Program in the Biomedical Sciences. We also thank Dr.
649 Lixin Fan of the Small-Angle X-ray Scattering Core Facility, National Cancer Institute,
650 Frederick, MD for acquiring the SAXS data.
651
652

653 References

654 Alekshun MN, Levy SB. 1999. Characterization of MarR superrepressor mutants. *J Bacteriol.*
655 181:3303-3306.

656 Alekshun MN, Levy SB. 2007. Molecular mechanisms of antibacterial multidrug resistance.
657 *Cell.* 128:1037-1050.

658 Alekshun MN, Levy SB, Mealy TR, Seaton BA, Head JF. 2001. The crystal structure of MarR, a
659 regulator of multiple antibiotic resistance, at 2.3 Å resolution. *Nat Struct Biol.* 8:710-714.

660 Anandapadamanaban M, Pilstål R, Andresen C, Trehewella J, Moche M, Wallner B, Sunnerhagen
661 M. 2016. Mutation-induced population shift in the MexR conformational ensemble
662 disengages DNA binding: A novel mechanism for MarR family derepression. *Structure.*
663 24:1311-1321.

664 Anderson KM, Esadze A, Manoharan M, Brüschweiler R, Gorenstein DG, Iwahara J. 2013.
665 Direct observation of the ion-pair dynamics at a protein–DNA interface by NMR
666 spectroscopy. *J Am Chem Soc.* 135:3613-3619.

667 Andresen C, Jalal S, Aili D, Wang Y, Islam S, Jarl A, Liedberg B, Wretlind B, Martensson LG,
668 Sunnerhagen M. 2010. Critical biophysical properties in the *Pseudomonas aeruginosa*
669 efflux gene regulator MexR are targeted by mutations conferring multidrug resistance.
670 *Protein Sci.* 19:680-692.

671 Aranda J, Garrido ME, Fittipaldi N, Cortes P, Llagostera M, Gottschalk M, Barbe J. 2009.
672 Protective capacities of cell surface-associated proteins of *Streptococcus suis* mutants
673 deficient in divalent cation-uptake regulators. *Microbiology.* 155:1580-1587.

674 Arunkumar AI, Pennella MA, Kong X, Giedroc DP. 2007. Resonance assignments of the metal
675 sensor CzrA in the apo-, Zn₂- and DNA-bound (42 kDa) states. *Biomol NMR Assign.*
676 1:99-101.

677 Birukou I, Seo SM, Schindler BD, Kaatz GW, Brennan RG. 2014. Structural mechanism of
678 transcription regulation of the *Staphylococcus aureus* multidrug efflux operon *mepRA* by
679 the MarR family repressor MepR. *Nucleic Acids Res.* 42:2774-2788.

680 Bordelon T, Wilkinson SP, Grove A, Newcomer ME. 2006. The crystal structure of the
681 transcriptional regulator HucR from *Deinococcus radiodurans* reveals a repressor
682 preconfigured for DNA binding. *J Mol Biol.* 360:168-177.

683 Campanello GC, Ma Z, Grossoeohme NE, Guerra AJ, Ward BP, Dimarchi RD, Ye Y, Dann III
684 CE, Giedroc DP. 2013. Allosteric inhibition of a zinc-sensing transcriptional repressor:
685 Insights into the arsenic repressor (ArsR) family. *J Mol Biol.* 425:1143-1157.

686 Campbell E, Kaltenbach M, Correy GJ, Carr PD, Porebski BT, Livingstone EK, Afriat-Jurnou L,
687 Buckle AM, Weik M, Hollfelder F, Tokuriki N, Jackson CJ. 2016. The role of protein
688 dynamics in the evolution of new enzyme function. *Nat Chem Biol.* 12:944-950.

689 Capdevila DA, Braymer JJ, Edmonds KA, Wu H, Giedroc DP. 2017a. Entropy redistribution
690 controls allostery in a metalloregulatory protein. *Proc Natl Acad Sci U S A.* 114:4424-
691 4429.

692 Capdevila DA, Edmonds KA, Giedroc DP. 2017b. Metallochaperones and metalloregulation in
693 bacteria. *Essays Biochem.* 61:177-200.

694 Caro JA, Harpole KW, Kasinath V, Lim J, Granja J, Valentine KG, Sharp KA, Wand AJ. 2017.
695 Entropy in molecular recognition by proteins. *Proc Natl Acad Sci U S A.* 114:6563-6568.

696 Chakravorty DK, Parker TM, Guerra AJ, Sherrill CD, Giedroc DP, Merz KM, Jr. 2013.
697 Energetics of zinc-mediated interactions in the allosteric pathways of metal sensor
698 proteins. *J Am Chem Soc.* 135:30-33.

699 Chang YM, Jeng WY, Ko TP, Yeh YJ, Chen CK, Wang AH. 2010. Structural study of TcaR and
700 its complexes with multiple antibiotics from *Staphylococcus epidermidis*. Proc Natl Acad
701 Sci U S A. 107:8617-8622.

702 Chen PR, Bae T, Williams WA, Duguid EM, Rice PA, Schneewind O, He C. 2006. An
703 oxidation-sensing mechanism is used by the global regulator MgrA in *Staphylococcus*
704 *aureus*. Nat Chem Biol. 2:591-595.

705 Chin KH, Tu ZL, Li JN, Chou CC, Wang AH, Chou SH. 2006. The crystal structure of XC1739:
706 a putative multiple antibiotic-resistance repressor (MarR) from *Xanthomonas campestris*
707 at 1.8 Å resolution. Proteins. 65:239-242.

708 Clarke D, Sethi A, Li S, Kumar S, Chang RW, Chen J, Gerstein M. 2016. Identifying allosteric
709 hotspots with dynamics: Application to inter- and intra-species conservation. Structure.
710 24:826-837.

711 Cohen SP, Hachler H, Levy SB. 1993. Genetic and functional analysis of the multiple antibiotic
712 resistance (*mar*) locus in *Escherichia coli*. J Bacteriol. 175:1484-1492.

713 Delaglio F, Grzesiek S, Vuister GW, Zhu G, Pfeifer J, Bax A. 1995. NMRPipe: A
714 multidimensional spectral processing system based on UNIX pipes. J Biomol NMR.
715 6:277-293.

716 Deochand DK, Grove A. 2017. MarR family transcription factors: Dynamic variations on a
717 common scaffold. Crit Rev Biochem Mol Biol. 52:595-613.

718 Deochand DK, Perera IC, Crochet RB, Gilbert NC, Newcomer ME, Grove A. 2016. Histidine
719 switch controlling pH-dependent protein folding and DNA binding in a transcription
720 factor at the core of synthetic network devices. Mol BioSyst. 12:2417-2426.

721 Dolan KT, Duguid EM, He C. 2011. Crystal structures of SlyA protein, a master virulence
722 regulator of *Salmonella*, in free and DNA-bound states. J Biol Chem. 286:22178-22185.

723 Dosset P, Hus JC, Blackledge M, Marion D. 2000. Efficient analysis of macromolecular
724 rotational diffusion from heteronuclear relaxation data. J Biomol NMR. 16:23-28.

725 Duval V, McMurry LM, Foster K, Head JF, Levy SB. 2013. Mutational analysis of the multiple-
726 antibiotic resistance regulator marR reveals a ligand binding pocket at the interface
727 between the dimerization and DNA binding domains. J Bacteriol. 195:3341-3351.

728 Ellison DW, Miller VL. 2006. Regulation of virulence by members of the MarR/SlyA family.
729 Curr Opin Microbiol. 9:153-159.

730 Franke D, Svergun DI. 2009. DAMMIF, a program for rapid *ab-initio* shape determination in
731 small-angle scattering. J Appl Crystallogr. 42:342-346.

732 Frederick KK, Marlow MS, Valentine KG, Wand AJ. 2007. Conformational entropy in
733 molecular recognition by proteins. Nature. 448:325-329.

734 Fuangthong M, Helmann JD. 2002. The OhrR repressor senses organic hydroperoxides by
735 reversible formation of a cysteine-sulfenic acid derivative. Proc Natl Acad Sci U S A.
736 99:6690-6695.

737 Gao YR, Li DF, Fleming J, Zhou YF, Liu Y, Deng JY, Zhou L, Zhou J, Zhu GF, Zhang XE,
738 Wang DC, Bi LJ. 2017. Structural analysis of the regulatory mechanism of MarR protein
739 Rv2887 in *M. tuberculosis*. Sci Rep. 7:6471.

740 Giedroc DP, Arunkumar AI. 2007. Metal sensor proteins: Nature's metalloregulated allosteric
741 switches. Dalton Trans. 29:3107-3120.

742 Goddard TD, Kneller DG, Sparky 3. University of California, San Francisco.

743 Grove A. 2013. MarR family transcription factors. Curr Biol. 23:R142-R143.

744 Grove A. 2017. Regulation of metabolic pathways by MarR family transcription factors. Comput
745 Struct Biotechnol J. 15:366-371.

746 Guerra AJ, Dann CE, Giedroc DP. 2011. Crystal structure of the zinc-dependent MarR family
747 transcriptional regulator AdcR in the Zn(II)-bound state. *J Am Chem Soc.* 133:19614-
748 19617.

749 Guerra AJ, Giedroc DP. 2014. Backbone and sterospecific methyl side chain resonance
750 assignments of the homodimeric zinc sensor AdcR (32 kDa) in the apo- and Zn(II)-bound
751 states. *Biomol NMR Assign.* 8:11-14.

752 Gupta A, Grove A. 2014. Ligand-binding pocket bridges DNA-binding and dimerization
753 domains of the urate-responsive MarR homologue MftR from *Burkholderia*
754 *thailandensis*. *Biochemistry.* 53:4368-4380.

755 Hao Z, Lou H, Zhu R, Zhu J, Zhang D, Zhao BS, Zeng S, Chen X, Chan J, He C, Chen PR.
756 2013. The multiple antibiotic resistance regulator MarR is a copper sensor in *Escherichia*
757 *coli*. *Nat Chem Biol.* 10:21-28.

758 Hong M, Fuangthong M, Helmann JD, Brennan RG. 2005. Structure of an OhrR-ohrA operator
759 complex reveals the DNA binding mechanism of the MarR family. *Mol Cell.* 20:131-141.

760 Hyberts SG, Milbradt AG, Wagner AB, Arthanari H, Wagner G. 2012. Application of iterative
761 soft thresholding for fast reconstruction of NMR data non-uniformly sampled with
762 multidimensional Poisson Gap scheduling. *J Biomol NMR.* 52:315-327.

763 Igumenova TI, Frederick KK, Wand AJ. 2006. Characterization of the fast dynamics of protein
764 amino acid side chains using NMR relaxation in solution. *Chem Rev.* 106:1672-1699.

765 Kalodimos CG, Biris N, Bonvin AM, Levandoski MM, Guennuegues M, Boelens R, Kaptein R.
766 2004. Structure and flexibility adaptation in nonspecific and specific protein-DNA
767 complexes. *Science.* 305:386-389.

768 Kim Y, Joachimiak G, Bigelow L, Babbitt G, Joachimiak A. 2016. How aromatic compounds
769 block DNA binding of HcaR catabolite regulator. *J Biol Chem.* 291:13243-13256.

770 Korzhnev DM, Kloiber K, Kanelis V, Tugarinov V, Kay LE. 2004. Probing slow dynamics in
771 high molecular weight proteins by methyl-TROSY NMR spectroscopy: application to a
772 723-residue enzyme. *J Am Chem Soc.* 126:3964-3973.

773 Kuzmic P. 1996. Program DYNAFIT for the analysis of enzyme kinetic data: application to HIV
774 proteinase. *Anal Biochem.* 237:260-273.

775 Lee W, Tonelli M, Markley JL. 2015. NMRFAM-SPARKY: enhanced software for
776 biomolecular NMR spectroscopy. *Bioinformatics.* 31:1325-1327.

777 Liguori A, Malito E, Lo Surdo P, Fagnocchi L, Cantini F, Haag AF, Brier S, Pizza M, Delany I,
778 Bottomley MJ. 2016. Molecular basis of ligand-dependent regulation of NadR, the
779 transcriptional repressor of meningococcal virulence factor NadA. *PLoS Pathog.*
780 12:e1005557.

781 Liu G, Liu X, Xu H, Liu X, Zhou H, Huang Z, Gan J, Chen H, Lan L, Yang CG. 2017. Structural
782 insights into the redox-sensing mechanism of MarR-type regulator AbfR. *J Am Chem*
783 *Soc.* 139:1598-1608.

784 Llull D, Son O, Blanier S, Briffaut J, Morello E, Rogniaux H, Danot O, Poquet I. 2011.
785 *Lactococcus lactis* ZitR is a zinc-responsive repressor active in the presence of low,
786 nontoxic zinc concentrations in vivo. *J Bacteriol.* 193:1919-1929.

787 Loo CY, Mitrakul K, Voss IB, Hughes CV, Ganeshkumar N. 2003. Involvement of the *adc*
788 operon and manganese homeostasis in *Streptococcus gordonii* biofilm formation. *J*
789 *Bacteriol.* 185:2887-2900.

790 Marijuan PC, Navarro J, del Moral R. 2010. On prokaryotic intelligence: strategies for sensing
791 the environment. *Biosystems.* 99:94-103.

792 Motlagh HN, Wrabl JO, Li J, Hilser VJ. 2014. The ensemble nature of allostery. *Nature*.
793 508:331-339.

794 Otani H, Stogios PJ, Xu X, Nocek B, Li SN, Savchenko A, Eltis LD. 2016. The activity of
795 CouR, a MarR family transcriptional regulator, is modulated through a novel molecular
796 mechanism. *Nucleic Acids Res*. 44:595-607.

797 Pabis A, Risso VA, Sanchez-Ruiz JM, Kamerlin SC. 2018. Cooperativity and flexibility in
798 enzyme evolution. *Curr Opin Struct Biol*. 48:83-92.

799 Peng H, Zhang Y, Palmer LD, Kehl-Fie TE, Skaar EP, Trinidad JC, Giedroc DP. 2017.
800 Hydrogen sulfide (H₂S) and reactive sulfur species (RSS) impact proteome S-
801 sulphydratation and global virulence regulation in *Staphylococcus aureus*. *ACS Infect*
802 *Dis*. 3:744-755.

803 Perera IC, Grove A. 2010. Molecular mechanisms of ligand-mediated attenuation of DNA
804 binding by MarR family transcriptional regulators. *J Mol Cell Biol*. 2:243-254.

805 Perez-Rueda E, Collado-Vides J, Segovia L. 2004. Phylogenetic distribution of DNA-binding
806 transcription factors in bacteria and archaea. *Comput Biol Chem*. 28:341-350.

807 Quade N, Mendonca C, Herbst K, Heroven AK, Ritter C, Heinz DW, Dersch P. 2012. Structural
808 basis for intrinsic thermosensing by the master virulence regulator RovA of *Yersinia*. *J*
809 *Biol Chem*. 287:35796-35803.

810 Radhakrishnan A, Kumar N, Wright CC, Chou TH, Tringides ML, Bolla JR, Lei HT,
811 Rajashankar KR, Su CC, Purdy GE, Yu EW. 2014. Crystal structure of the transcriptional
812 regulator Rv0678 of *Mycobacterium tuberculosis*. *J Biol Chem*. 289:16526-16540.

813 Reyes-Caballero H, Guerra AJ, Jacobsen FE, Kazmierczak KM, Cowart D, Koppolu UM, Scott
814 RA, Winkler ME, Giedroc DP. 2010. The metalloregulatory zinc site in *Streptococcus*
815 *pneumoniae* AdcR, a zinc-activated MarR family repressor. *J Mol Biol*. 403:197-216.

816 Sanson M, Makthal N, Flores AR, Olsen RJ, Musser JM, Kumaraswami M. 2015. Adhesin
817 competence repressor (AdcR) from *Streptococcus pyogenes* controls adaptive responses
818 to zinc limitation and contributes to virulence. *Nucleic Acids Res*. 43:418-432.

819 Saridakis V, Shahinas D, Xu X, Christendat D. 2008. Structural insight on the mechanism of
820 regulation of the MarR family of proteins: high-resolution crystal structure of a
821 transcriptional repressor from *Methanobacterium thermoautotrophicum*. *J Mol Biol*.
822 377:655-667.

823 Schneidman-Duhovny D, Hammel M, Sali A. 2010. FoXS: a web server for rapid computation
824 and fitting of SAXS profiles. *Nucleic Acids Res*. 38:W540-544.

825 Seoane AS, Levy SB. 1995. Characterization of MarR, the repressor of the multiple antibiotic
826 resistance (*mar*) operon in *Escherichia coli*. *J Bacteriol*. 177:3414-3419.

827 Shen Y, Delaglio F, Cornilescu G, Bax A. 2009. TALOS+: a hybrid method for predicting
828 protein backbone torsion angles from NMR chemical shifts. *J Biomol NMR*. 44:213-223.

829 Sun F, Ding Y, Ji Q, Liang Z, Deng X, Wong CC, Yi C, Zhang L, Xie S, Alvarez S, Hicks LM,
830 Luo C, Jiang H, Lan L, He C. 2012. Protein cysteine phosphorylation of SarA/MgrA
831 family transcriptional regulators mediates bacterial virulence and antibiotic resistance.
832 *Proc Natl Acad Sci U S A*. 109:15461-15466.

833 Takano H, Mise K, Maruyama T, Hagiwara K, Ueda K. 2016. Role of the semi-conserved
834 histidine residue in the light-sensing domain of LitR, a MerR-type photosensory
835 transcriptional regulator. *Microbiology*. 162:1500-1509.

836 Tamber S, Cheung AL. 2009. SarZ promotes the expression of virulence factors and represses
837 biofilm formation by modulating SarA and *agr* in *Staphylococcus aureus*. *Infect Immun*.
838 77:419-428.

839 Tollinger M, Skrynnikov NR, Mulder FAA, Forman-Kay JD, Kay LE. 2001. Slow dynamics in
840 folded and unfolded states of an SH3 domain. *J Am Chem Soc.* 123:11341-11352.

841 Tugarinov V, Kay LE. 2003. Ile, Leu, and Val methyl assignments of the 723-Residue malate
842 synthase G using a new labeling strategy and novel NMR methods. *J Am Chem Soc*
843 125:13868-13878.

844 Tugarinov V, Kay LE. 2004. ^1H , ^{13}C - ^1H , ^1H dipolar cross-correlated spin relaxation in methyl
845 groups. *J Biomol NMR.* 29:369-376.

846 Tugarinov V, Sprangers R, Kay LE. 2007. Probing side-chain dynamics in the proteasome by
847 relaxation violated coherence transfer NMR spectroscopy. *J Am Chem Soc.* 129:1743-
848 1750.

849 Tzeng SR, Kalodimos CG. 2009. Dynamic activation of an allosteric regulatory protein. *Nature.*
850 462:368-372.

851 Tzeng SR, Kalodimos CG. 2012. Protein activity regulation by conformational entropy. *Nature.*
852 488:236-240.

853 Tzeng SR, Kalodimos CG. 2013. Allosteric inhibition through suppression of transient
854 conformational states. *Nat Chem Biol.* 9:462-465.

855 Ulrich LE, Koonin EV, Zhulin IB. 2005. One-component systems dominate signal transduction
856 in prokaryotes. *Trends Microbiol.* 13:52-56.

857 Weatherspoon-Griffin N, Wing HJ. 2016. Characterization of SlyA in *Shigella flexneri* identifies
858 a novel role in virulence. *Infect Immun.* 84:1073-1082.

859 West AL, Evans SE, Gonzalez JM, Carter LG, Tsuruta H, Pozharski E, Michel SL. 2012. Ni(II)
860 coordination to mixed sites modulates DNA binding of HpNikR via a long-range effect.
861 *Proc Natl Acad Sci U S A.* 109:5633-5638.

862 Wilke MS, Heller M, Creagh AL, Haynes CA, McIntosh LP, Poole K, Strynadka NCJ. 2008.
863 The crystal structure of MexR from *Pseudomonas aeruginosa* in complex with its
864 antirepressor ArmR. *Proc Natl Acad Sci U S A.* 105:14832-14837.

865 Wishart DS, Sykes BD. 1994. Chemical shifts as a tool for structure determination. *Methods
866 Enzymol.* 239:363-392.

867 Yoon H, McDermott JE, Porwollik S, McClelland M, Heffron F. 2009. Coordinated regulation
868 of virulence during systemic infection of *Salmonella enterica* serovar Typhimurium.
869 *PLoS Pathog.* 5:e1000306.

870 Zhu R, Hao Z, Lou H, Song Y, Zhao J, Chen Y, Zhu J, Chen PR. 2017a. Structural
871 characterization of the DNA-binding mechanism underlying the copper(II)-sensing MarR
872 transcriptional regulator. *J Biol Inorg Chem.* 22:685-693.

873 Zhu R, Hao Z, Lou H, Song Y, Zhao J, Zhu J, Chen PR. 2017b. Structural and mechanistic study
874 of the cysteine oxidation-mediated induction of the *Escherichia coli* MarR regulator.
875 *Tetrahedron.* 73:3714-3719.

876 Zhu R, Song Y, Liu H, Yang Y, Wang S, Yi C, Chen PR. 2017c. Allosteric histidine switch for
877 regulation of intracellular zinc(II) fluctuation. *Proc Natl Acad Sci U S A.* 114:13661-
878 13666.

879

880

881 **Figure Legends**

882
883

884 **Figure 1.** (a) Ribbon representation of dimeric Zn(II)-bound AdcR, with one protomer shaded
885 white and the other shaded *light blue* (PDB-ID: 3tgn) (Guerra *et al.*, 2011). The two Zn(II) ions
886 in each protomer are represented by spheres, and coordinating ligands are shown in stick
887 representation. The DNA binding helices are shaded *red*. (b) Simplified free energy diagram
888 showing of the active (*green*) and inactive (*blue*) states the relative population of two distinct
889 conformations: compatible with DNA binding (*red* rectangle, $\alpha 4$ - $\alpha 4'$ distance between DNA
890 binding helices, ≈ 30 Å) and incompatible with DNA binding (larger $\alpha 4$ - $\alpha 4'$ distances). (c) The
891 $\alpha 4$ - $\alpha 4'$ distance distribution plotted against the DNA-binding inter-helical $\alpha 4$ - $\alpha 4'$ orientation
892 distribution for all the reported MarR crystal structures (see Table S1 for details) in the
893 allosterically “active” DNA-binding conformation (*green*), an “inactive” conformation (*blue*)
894 and in the DNA-bound (*red*) conformation. The inferred conformational space occupied by the
895 DNA-bound conformation in all MarR regulators (Table S1) is shaded in *red* oval. Ribbon
896 representation of the molecules in each conformation are shown in the inset, as well as a scheme
897 of how the distances and angles were measured. (d) Histogram plot of the $\alpha 4$ - $\alpha 4'$ distance (see
898 panel c) extracted from 136 different crystal structures of MarR repressors in the DNA-binding-
899 “inactive”, DNA-binding “active” and DNA-bound conformations.

900

901 **Figure 2.** (a) Small angle X-ray scattering (SAXS) curve of AdcR in apo- and Zn₂-states, with a
902 curve calculated from the previously published AdcR-Zn₂ structure (Fig. 1A, PDB-ID: 3tgn)
903 (Guerra *et al.*, 2011). Best-fit DAMMIF *ab initio* model(Franke & Svergun, 2009) for apo- (b)
904 (blue) and Zn^{II}₂-states (c) (green), aligned with the ribbon representation of the Zn^{II}₂ structure

905 (Fig. 1A, PDB-ID: 3tgn). The corresponding Guinier, Kratky and pairwise distribution
906 histogram plots are shown in Fig. S2, along with the fitting parameters.

907

908 **Figure 3.** Chemical shift perturbation maps for Zn^{II} binding to AdcR for the backbone (a) and
909 the sterospecifically assigned methyl groups (b) at pH 5.5, 50 mM NaCl, 35 °C. CSPs are
910 painted on the ribbon representation of the structure of $Zn^{II}2$ AdcR. The shaded bar in each case
911 represents one standard deviation from the mean perturbation. Site 1 and site 2 ligands in the
912 primary structure in panel (a) are denoted by the *yellow* and *green* circles, respectively; the
913 asterisks at residue positions 21 and 38-40 indicate no assignment in the apo-state (see Materials
914 and Methods). (c) Distribution of $\alpha1-\alpha2$ loops lengths in the reported structures in all MarR
915 family of proteins (see Table S1 for an accounting of these structures). A postulated schematic
916 representation of allosteric inhibition and activation are shown (*inset*), with shorter $\alpha1-\alpha2$ loops
917 driving allosteric inhibition of the DNA binding upon ligand binding, and longer loops
918 associated with allosteric activation (like that for AdcR/ZitR) upon ligand binding.

919

920 **Figure 4.** Dynamical characterization of the apo- (a) (c) (e) and $Zn^{II}2$ (b) (d) (f) AdcR
921 conformational states. Backbone 1H - ^{15}N amide R_2/R_1 for apo- (a) and $Zn^{II}2$ AdcR (b) painted
922 onto the 3tgn structure (Guerra *et al.*, 2011). Heteronuclear NOE analysis of apo- (c) and $Zn^{II}2$
923 (d) AdcR with the values of the ^{15}N -{ 1H }-NOE (hNOE) painted onto the 3tgn structure. Values
924 of R_{ex} determined from HSQC ^{15}N - 1H CPMG relaxation dispersion experiments at a field of 600
925 MHz for the apo- (e) and $Zn^{II}2$ (f) AdcRs (see Fig. S6 for complete data). Similar results were
926 obtained at 800 MHz (Fig. S6). Zn^{II} ions are shown as black spheres and residues excluded due
927 to overlapped are shown in gray and yellow. The width of the ribbon reflects the value
928 represented in the color bar.

929

930 **Figure 5.** Effect of Zn^{II} binding to AdcR on the site-specific stereospecifically assigned methyl
931 group axial order parameter, S^2_{axis} (a) and R_{ex} (b) plotted as ΔS^2_{axis} ($S^2_{\text{axis}}^{\text{Zn}} - S^2_{\text{axis}}^{\text{apo}}$) and ΔR_{ex}
932 ($R_{\text{ex}}^{\text{Zn}} - R_{\text{ex}}^{\text{apo}}$) values, respectively, mapped onto the structure of Zn^{II}₂ AdcR (3tgn). A $\Delta S^2_{\text{axis}} < 0$
933 indicates that the methyl group becomes *more* dynamic in the Zn^{II}₂-bound state, while $\Delta R_{\text{ex}} < 0$
934 indicates quenching of motion on the $\mu\text{s-ms}$ timescale in the in the Zn^{II}₂-bound state. See Fig. S5
935 for a graphical representation of all S^2_{axis} and R_{ex} values in each conformation from which these
936 differences were determined, and Fig. S6 for summary of all dynamical parameters measured
937 here. Residues harboring methyl groups that show major dynamical perturbations on Zn^{II}
938 binding are highlighted, with selected residues subjected to cavity mutagenesis (Fig. 6; Table
939 S2).

940

941 **Figure 6.** Graphical summary of the functional properties of AdcR cavity and hydrogen bonding
942 mutants. (a) Zoom of the DNA binding domain (DBD) of one of the two Zn^{II}₂-bound AdcR
943 protomers highlighting the residues targeted for mutagenesis (cavity mutants, *red stick*;
944 hydrogen-bonding pathway mutants, *green stick*; zinc ligand E24, *yellow stick*), with the helical
945 elements ($\alpha 1$ - $\alpha 5$) indicated. (b) C α positions of the residues targeted for cavity mutagenesis in
946 the DNA binding domain (DBD) (*red spheres*) and in the dimerization domain (DIM) (*blue
947 spheres*); other residues targeted for substitution in the hydrogen-bonding pathway (N38, Q40;
948 *green spheres*) and zinc ligand E24 (*yellow spheres*) highlighted on the structure of the Zn^{II}₂
949 ZitR-DNA operator complex (Zhu *et al.*, 2017c); Zn^{II} ions (*black spheres*). (c) Coupling free
950 energy analysis for all AdcR mutants highlighted using the same color scheme as in panels (a),
951 (b). DBD, DNA-binding domain; DIM, dimerization domain; H-bond, hydrogen binding
952 mutants. Lower horizontal line, K_{DNA} for wild-type apo-AdcR; upper horizontal line, K_{DNA} for

953 wild-type Zn^{II}_2 AdcR, for reference. The trend in $\Delta S_{2\text{axis}}$ and ΔR_{ex} is qualitatively indicated
954 (see Table S2). These residues are conserved to various degrees in AdcR-like repressors (Fig.
955 S12).

956

957 **Figure 7.** Entropically driven model for how conformational dynamics can be harnessed to
958 evolve allosteric activation (*upper right*) vs. allosteric inhibition (*lower right*) in the same
959 molecular scaffold. This model suggests that dynamic properties of the active states have been
960 conserved to give rise to a more favorable conformational entropy. In the metalloregulatory
961 MarRs (AdcR, ZitR), the inactive state shows perturbed dynamics over a range of timescales;
962 apo-AdcR therefore exhibits low affinity for DNA. Metal ion (*yellow circle*) coordination
963 quenches both local and global modes in the dimerization domain and linkers, while inducing
964 conformational disorder in the DNA-binding domain that enhances DNA binding affinity, thus
965 stabilizing a conformation that has high affinity for DNA and giving rise to a favorable
966 conformational entropy. For prototypical MarRs, where the ligand (*yellow star*) is an allosteric
967 inhibitor, ligand binding narrows the conformational ensemble to a DNA-binding “inactive”
968 conformation decreasing the enthalpic contribution to DNA binding, while perturbing fast time
969 scale dynamics that give rise to an unfavorable conformational entropy for DNA-binding.

970

971

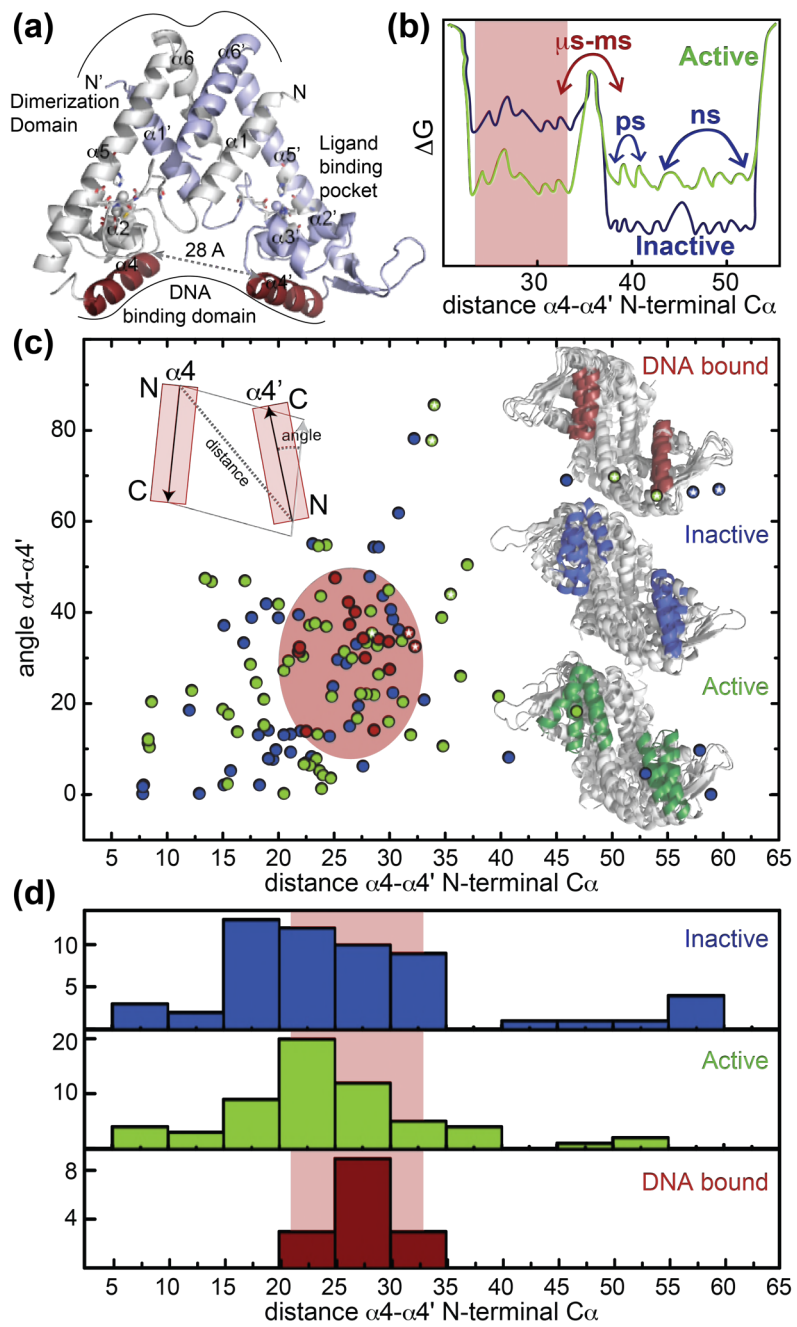
972

973

974

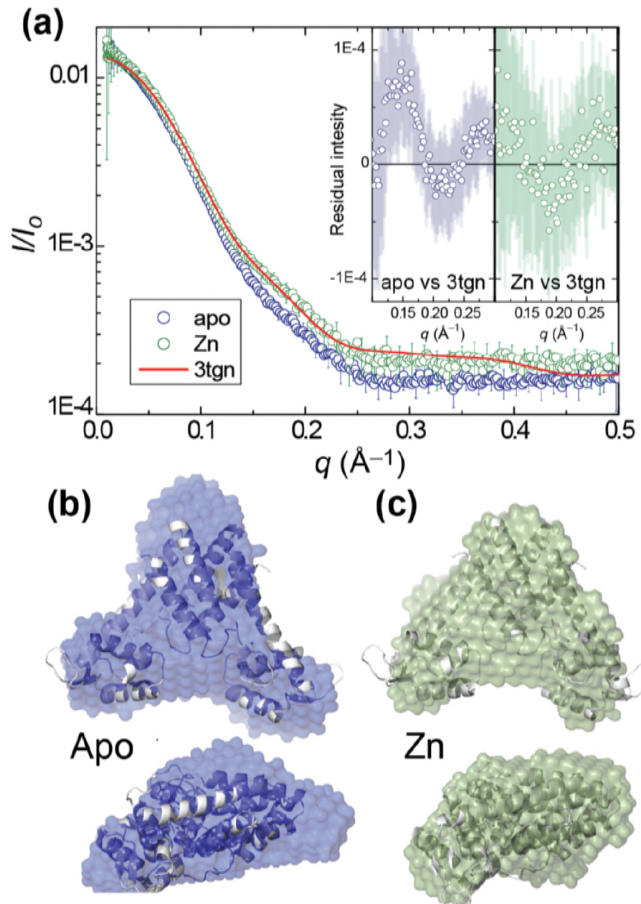
975 **FIGURES**

976 **Figure 1**

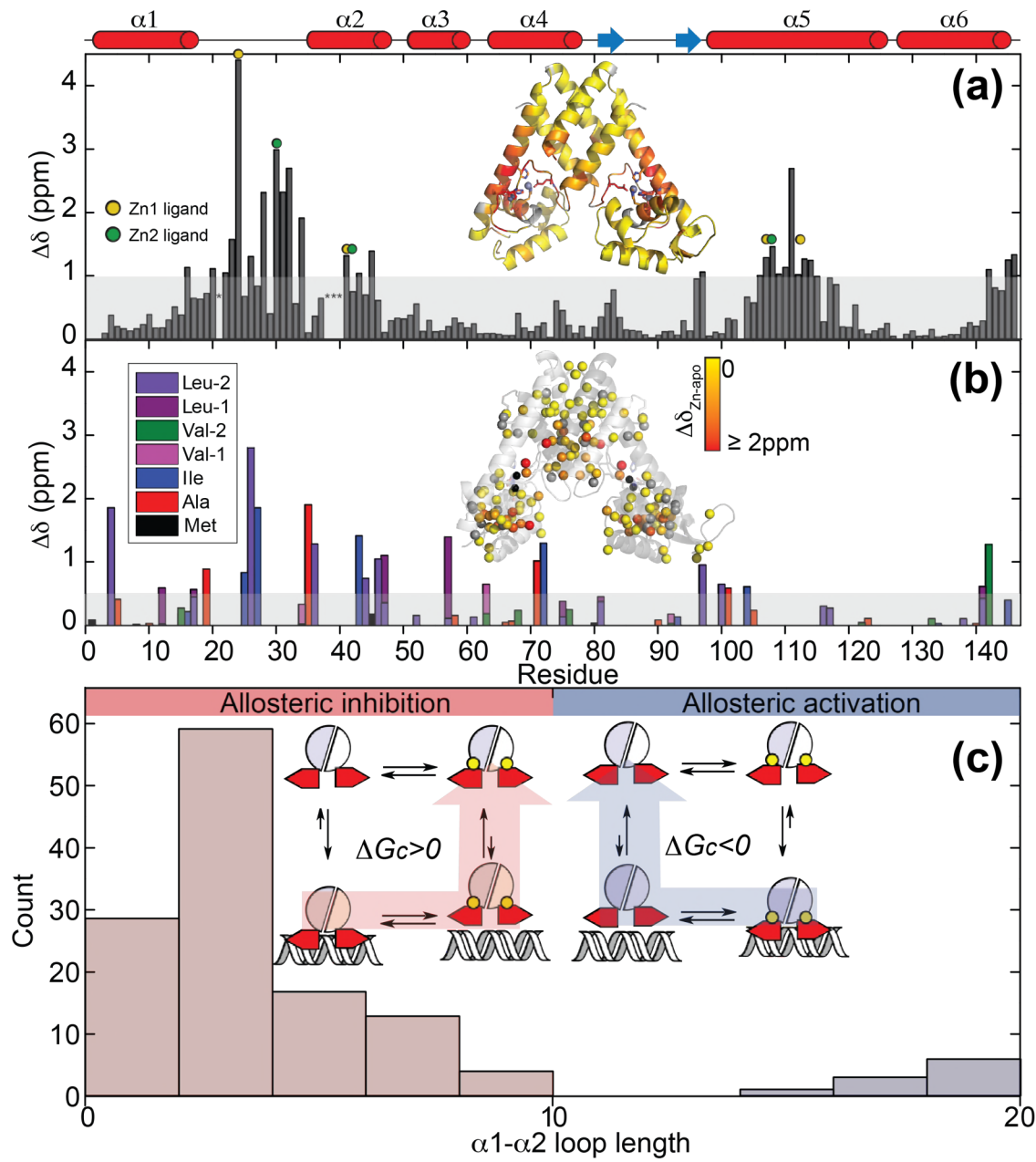


977

978 **Figure 2**

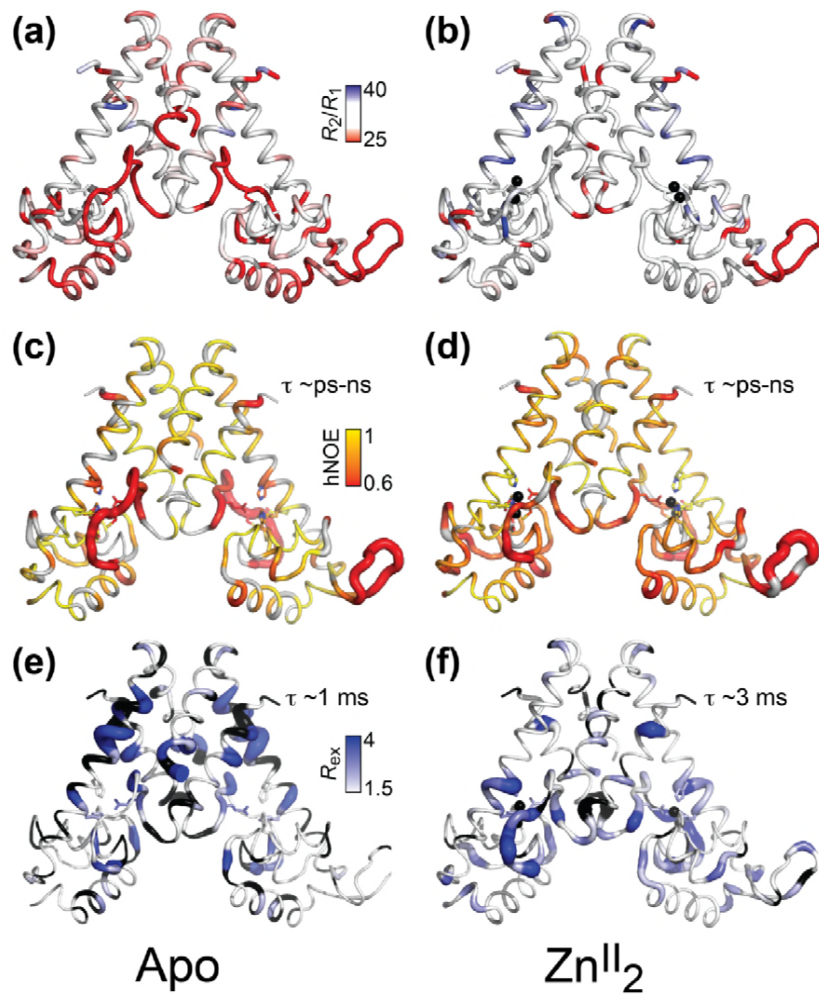


979 **Figure 3**



980

981 **Figure 4**

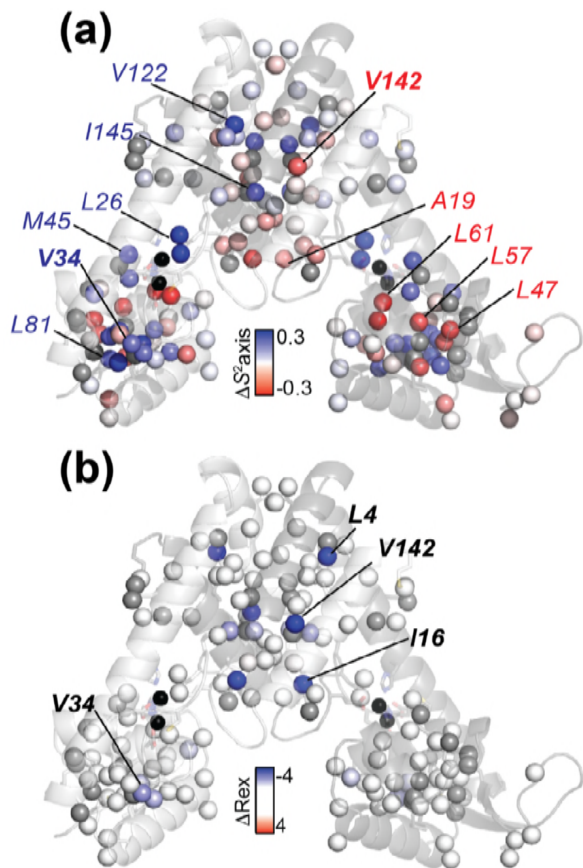


982

983

984

985 **Figure 5**



986

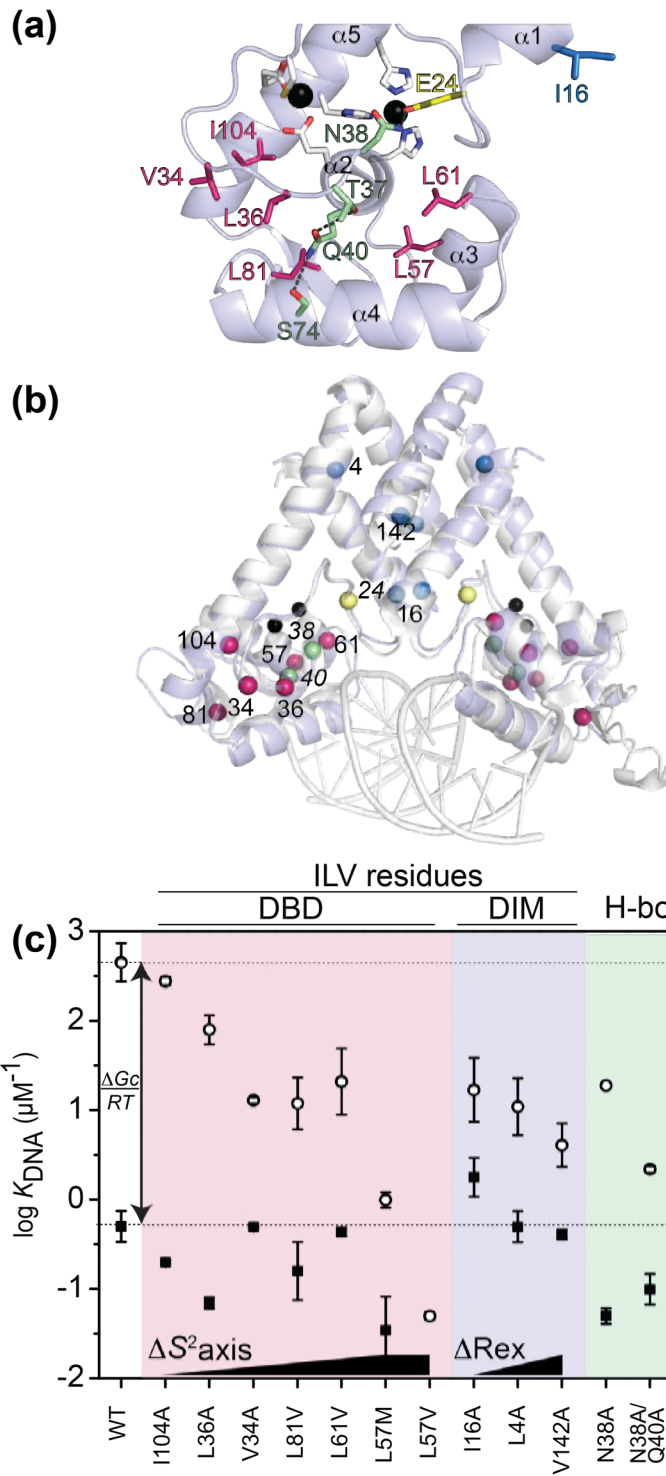
987

988

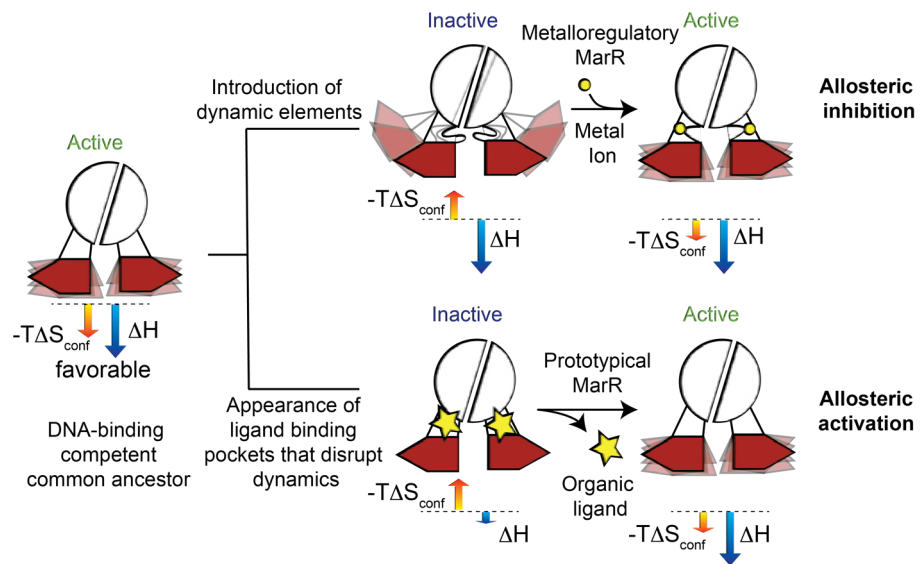
989 **Figure 6**

990

991



992 **Figure 7**



993

994

1

2 **Supplementary Data**

3

4 **Tuning site-specific dynamics to drive allosteric activation in a pneumococcal**
5 **zinc uptake regulator**

6

7 Daiana A. Capdevila,[†] Fidel Huerta,^{†,‡} Katherine A. Edmonds,[†] My T. Le,[†] Hongwei Wu,[†] and
8 David P. Giedroc^{*,†,§}

9

10 This file contains **Supplementary Tables S1-S3** and **Supplementary Figures S1-S12**.

11

12 **Table S1.** Interprotomer distances between the C α of the N-terminal residue in the $\alpha 4$ and $\alpha 4'$
13 helices

| MarR | DNA-bound state | | Inhibited state ^a | | Active state ^b | |
|----------------|-------------------|------------------|---------------------------------|-------------------------------|---|---|
| | Distance (Å) | PDB ID | Distance (Å) | PDB ID | Distance (Å) | PDB ID |
| ZitR (AdcR) | 32.3/31.7 | 5yi2/5yi3 | 59.6/57.3 | 5yh0/5yh1 | 35.5/54.0/ 50.2 (22.2/ 34/ 33.8) | 5yhx/5yhy/ 5yhz (3tgn/5jls/ 5jlu) |
| <i>Ec</i> MarR | 29 | 5hr3 | 12.9 / 12 | 1jgs/4jba | 8.3 / 8.4 | 3vod/3voe |
| OhrR | 27.6 | 1z9c | (32.2) | (2pfb) | 23.9 (28.9) | 1z91 (2pex) |
| SlyA | 27.8 | 3q5f | 29.4 | 3deu | 15.5 (23.8, 20) | 3qpt (1lj9, 4mnu) |
| AbsC | 26.3 | 3zpl | 30.8 | 3zmd | - | - |
| RovA | 21.8 / 21.9 | 4aij/ 4aik | - | - | 20.9 | 4aih |
| MosR | 25.1 | 4fx4 | 15.1 | 4fx0 | - | - |
| MepR | 26.4 / 26.9 | 4lll/ 4lln | 18.9/16.9/ 30.8/57.9 | 3eco/4l9n/ 4l9t/4l9v | 27.9 / 46.8 | 4l9j/4ld5 |
| AbfR | 29.9 / 30 | 5hlh/5hlg | 40.7 | 5hli | 37 | 4hbl |
| Rv2887 | 22.5 | 5hso | 7.9 / 15.1 | 5hsn/5hsl | 8.3 | 5hsm |
| HcaR | 28.6 | 5bmz | 19.1 / 19.8 / 19.5 / 19.2 | 4rgx /4rgu / 4rgs/ 4rgr | 18.7 | 3k0l |
| ST1710 | 10.1 ^c | 3gji | 23 | 3gf2 | 22.8 | 2eb7 |
| TcaR | 19.1 ^d | 4kd ^p | 22.3/24.7 | 4eju/3kp7 | 26.4/22.5/ 21.1/ 22/ 27.6/18.3/ 21.1/ 18.2 | 3kp2/ 3kp3/ 3kp4/ 3kp5/ 3kp7/ 4ejt/ 4ejv/ 4ejw |

14 ^aProposed or measured DNA binding constant below 10⁶ M⁻¹. ^b Proposed or measured DNA
15 binding constant above 10⁷ M⁻¹. ^c Not inserted in the major groove of the DNA. ^dThis structure
16 was co-crystallized with ssDNA.

17

18 **Table S2.** DNA binding parameters for wild-type AdcR and substitution mutants^a

| AdcR | $K_{\text{apo,DNA}}$ ($\times 10^6 \text{ M}^{-1}$) | Zn ^{II} | | Dynamic changes (Zn ^{II}) | | Fractional ASA ^b |
|-----------|--|---|---|-------------------------------------|--------------|--------------------------------|
| | | $K_{\text{Zn,DNA}}$ ($\times 10^6 \text{ M}^{-1}$) | ΔG_c (kcal mol ⁻¹) | ΔS^2_{axis} | ΔRex | |
| wild-type | 0.5 ± 0.2 | 450 ± 220 | -4.0 ± 0.6 | | | |
| I104A | 0.20 ± 0.01 | 280 ± 30 | -4.3 ± 0.4 | -0.08 ± 0.01 | 0.3 | 0.04 |
| L36A | 0.07 ± 0.01 | 80 ± 30 | -4.1 ± 0.4 | 0.15 ± 0.02 | 3.2 | 0.05 |
| V34A | $0.5^c \pm 0.01$ | 13 ± 1 | -2.2 ± 0.3 | 0.15 ± 0.02 | 3.5 | 0.46 |
| L81V | 0.16 ± 0.12 | 12 ± 8 | -2.4 ± 0.6 | 0.20 ± 0.02 | 0 | 0.00 |
| L61V | 0.44 ± 0.05 | 21 ± 18 | -2.3 ± 0.1 | -0.247 ± 0.001 | -0.7 | 0.01 |
| L57M | 0.035 ± 0.030 | 1 ± 0.2 | -2.0 ± 0.7 | -0.30 ± 0.02 | 0.7 | 0.00 |
| L57V | $<0.05^d$ | $<0.05^d$ | N/A | -0.30 ± 0.02 | 0.7 | 0.00 |
| I16A | 1.8 ± 0.9 | 17 ± 14 | -1.8 ± 0.4 | -0.07 ± 0.01 | 3.5 | 0.11 |
| L4A | 0.5 ± 0.2 | 11 ± 8 | -1.8 ± 0.3 | 0.02 ± 0.02 | 4 | 0.01 |
| V142A | 0.41 ± 0.05 | 4.1 ± 2.3 | -1.4 ± 0.2 | -0.095 ± 0.005 | 7 | 0.31 |
| N38A | 0.05 ± 0.01 | 19 ± 10 | -3.5 ± 0.7 | - ^e | - | - |
| N38A/Q40A | 0.10 ± 0.04 | 2.2 ± 0.4 | -1.9 ± 0.2 | - | - | - |
| E24D | 0.17 ± 0.04 | 2.2 ± 1.7 | -1.6 ± 0.3 | - | - | - |

19 ^aConditions: 10 mM Hepes, pH 7.0, 0.23 M NaCl, 1 mM TCEP (chelexed), 10 nM DNA, 25.0 °C
20 with 2.0 mM EDTA (for apo-AdcR) or 20 μM ZnCl₂ (for Zn^{II}₂ AdcR) added to these reactions.
21 See Fig. 6C, main text, for a graphical representation of these data. ^bAccessible surface area
22 (ASA) calculated from the Zn^{II}₂-bound AdcR (Guerra *et al.*, 2011). ^cUpper limit on measurable
23 $K_{\text{apo,DNA}}$ under these solution conditions. ^dWeaker than upper limit. ^eNot measurable using the
24 NMR experiments employed here.

25

26
27

Table S3. Zinc binding affinities of wild-type AdcR and selected AdcR mutants characterized here.

| AdcR | Zn ^{II} binding to site 2 in the homodimer | |
|-----------|---|---|
| | $K_{Zn,3}$ ($\times 10^9$ M ⁻¹) | $K_{Zn,4}$ ($\times 10^9$ M ⁻¹) |
| wild-type | ≥ 1 | 0.0205 ± 0.0013 |
| V34A | 0.0022 ± 0.0017 | $(9.4 \pm 8.2) \times 10^{-5}$ |
| L81V | ≥ 1 | 0.025 ± 0.0027 |
| L61V | ≥ 1 | 0.0181 ± 0.0022 |
| L57M | ≥ 1 | 0.0169 ± 0.001 |
| L57V | ≥ 1 | 0.119 ± 0.018 |
| I16A | ≥ 1 | 0.00479 ± 0.0005 |
| V142A | 0.00085 ± 0.00018 | $< 10^{-5}$ |

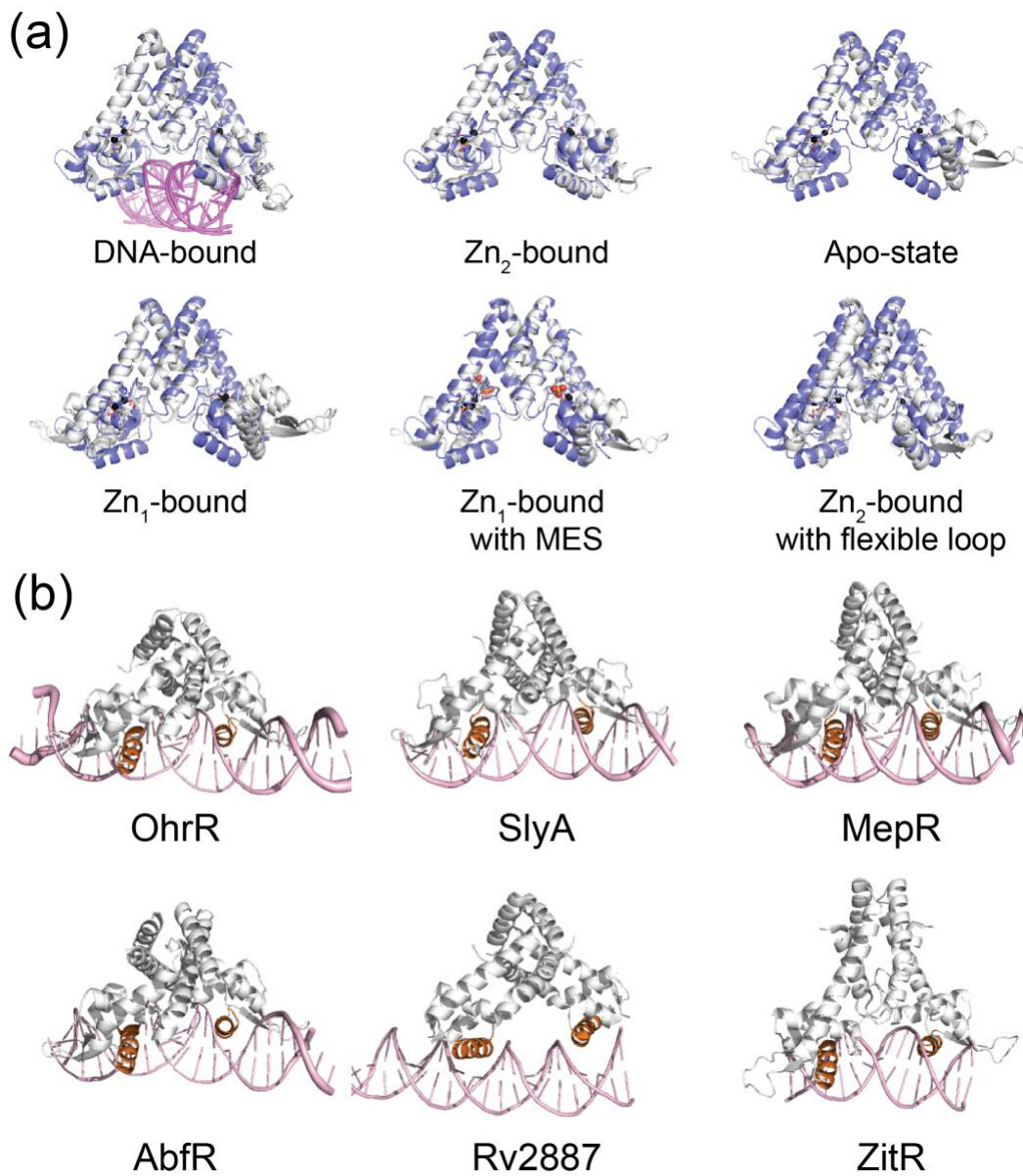
^aConditions: 10 mM Hepes, pH 7.2, 0.4 M NaCl, 1 mM TCEP (chelexed), 15 μ M Mf2, 25.0 °C titrated with ZnCl₂ solutions. Experiments were conducted 3 times for each AdcR variant. Errors of the binding constant parameters were estimated from global fits.

^b $K_{Zn,1}$ and $K_{Zn,2}$ were fixed to a value of 1×10^{12} M⁻¹. ^c $K_{Zn,Mf2} = (4.9 \pm 0.6) \times 10^6$ M⁻¹ under these solution conditions.

28
29
30
31
32
33
34
35

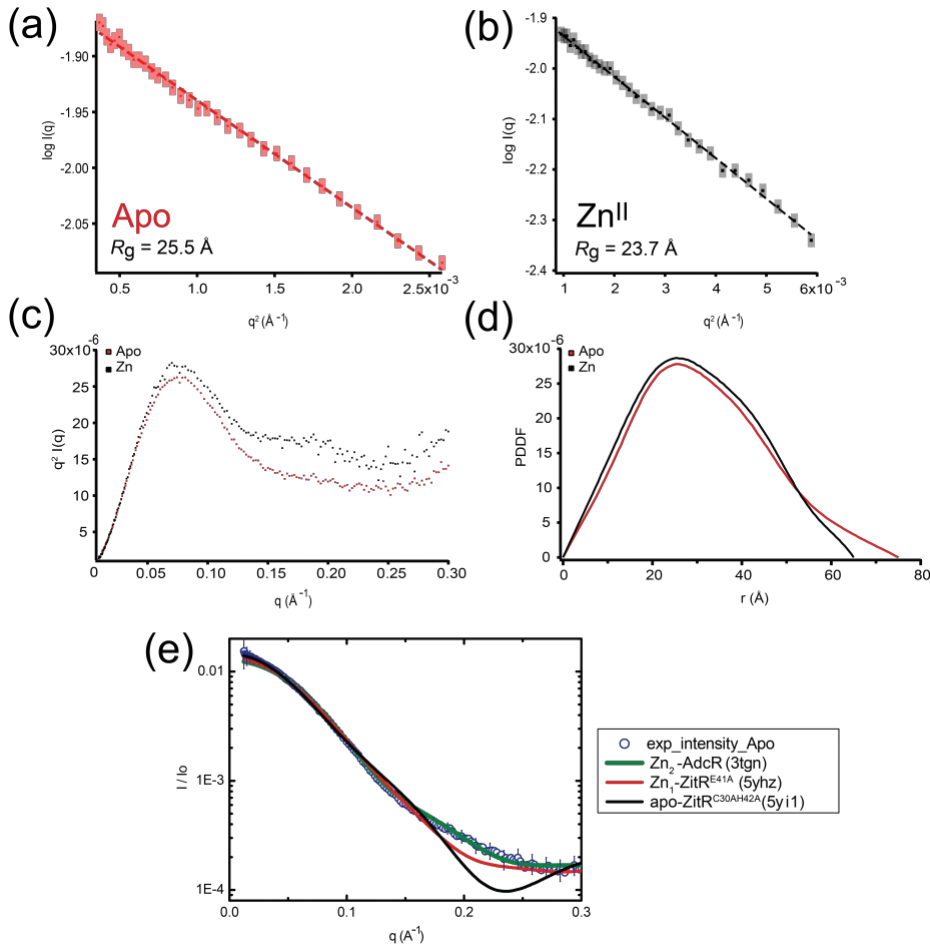
36

37
38

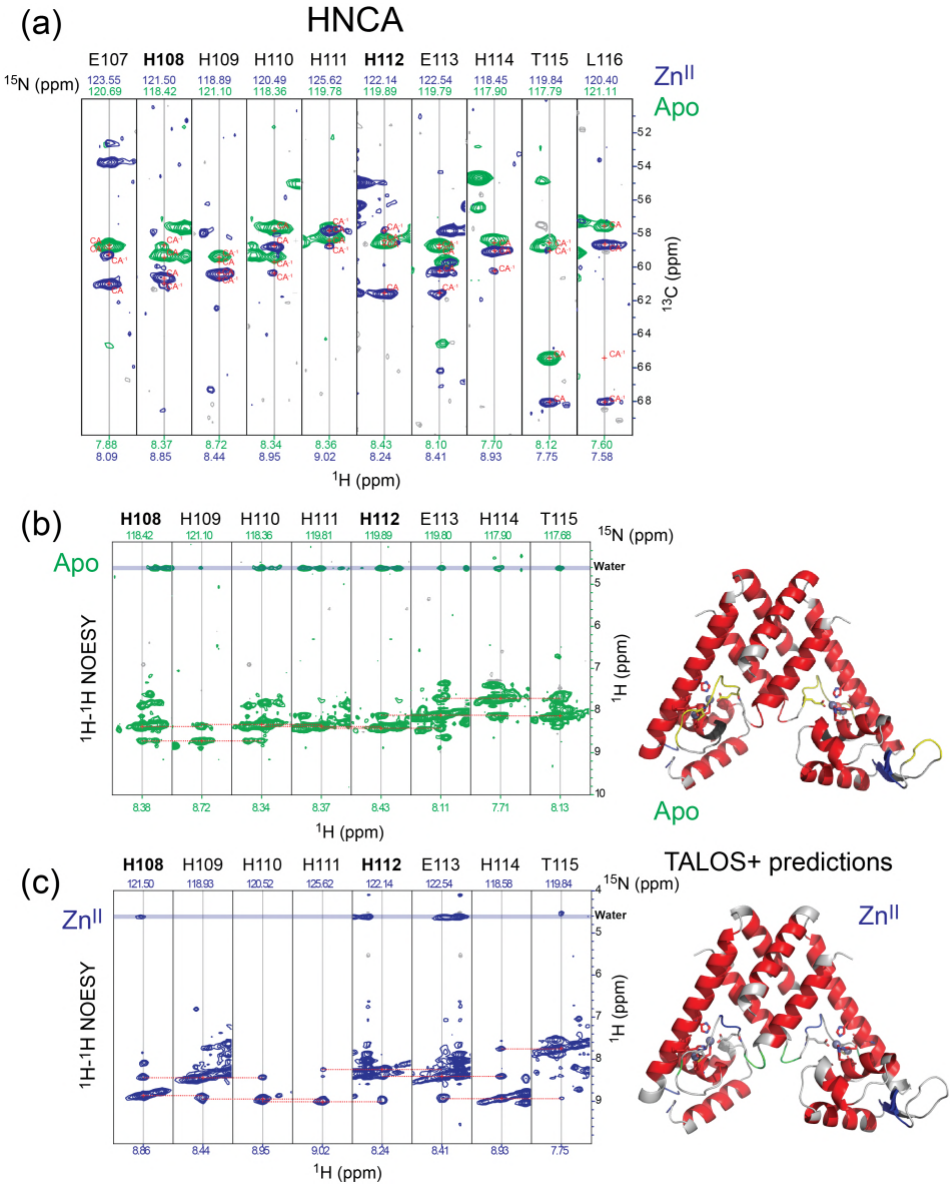


39 **Figure S1.** (a) Structural comparison (global superposition) between AdcR (3tgn, shaded slate in
40 all panels, (Guerra *et al.*, 2011)) and *L. lactis* ZitR (Zhu *et al.*, 2017) in the different allosteric
41 states (DNA-bound PDB codes, 5yi2, 5yi3; Zn^{II}₂-bound, 5hyx; Apo-state, 5yi1; Zn₁-bound PDB
42 ID 5yhy, 5yl0; Zn^{II}₂-bound alternative state with a MES molecule in Zn site 1, 5yhz; Zn₂-bound
43 from Group A *Streptococcus pyogenes* AdcR (Sanson *et al.*, 2015) with flexible loop, 5jls, 5lju).
44 (b) Structural comparisons of various MarR family repressors in the DNA-bound states. (*B.*
45 *subtilis* OhrR, PDB code, 1z9c; *S. enterica* SlyA, 3q5f; *S. aureus* MepR, 4lln; *S. epidermidis*
46 AbfR, 5hlg; *M. tuberculosis* Rv2887, 5hso; *L. Lactis* ZitR, 5yi2).

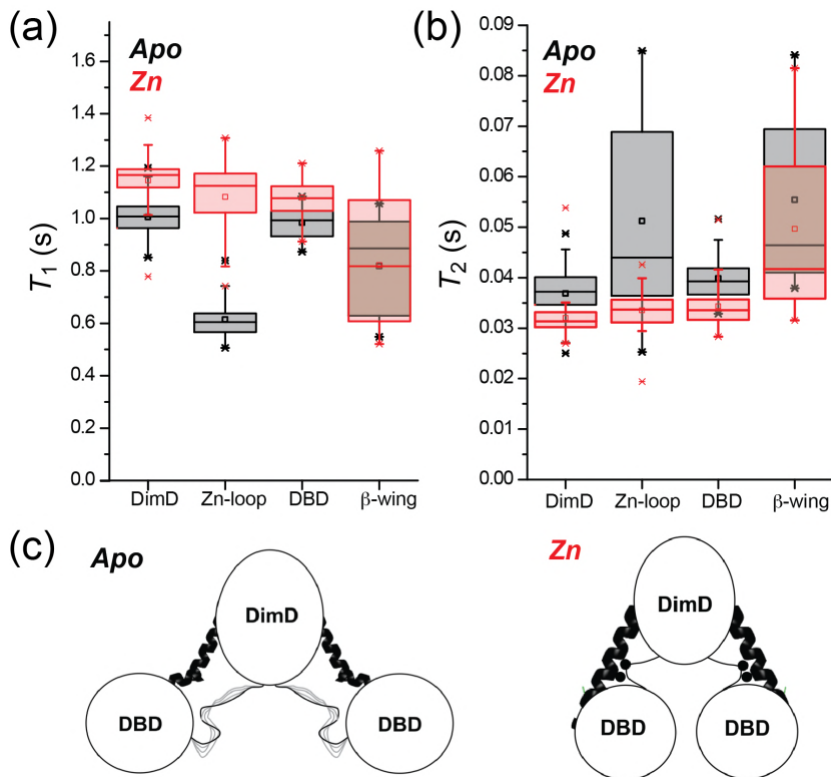
47
48
49



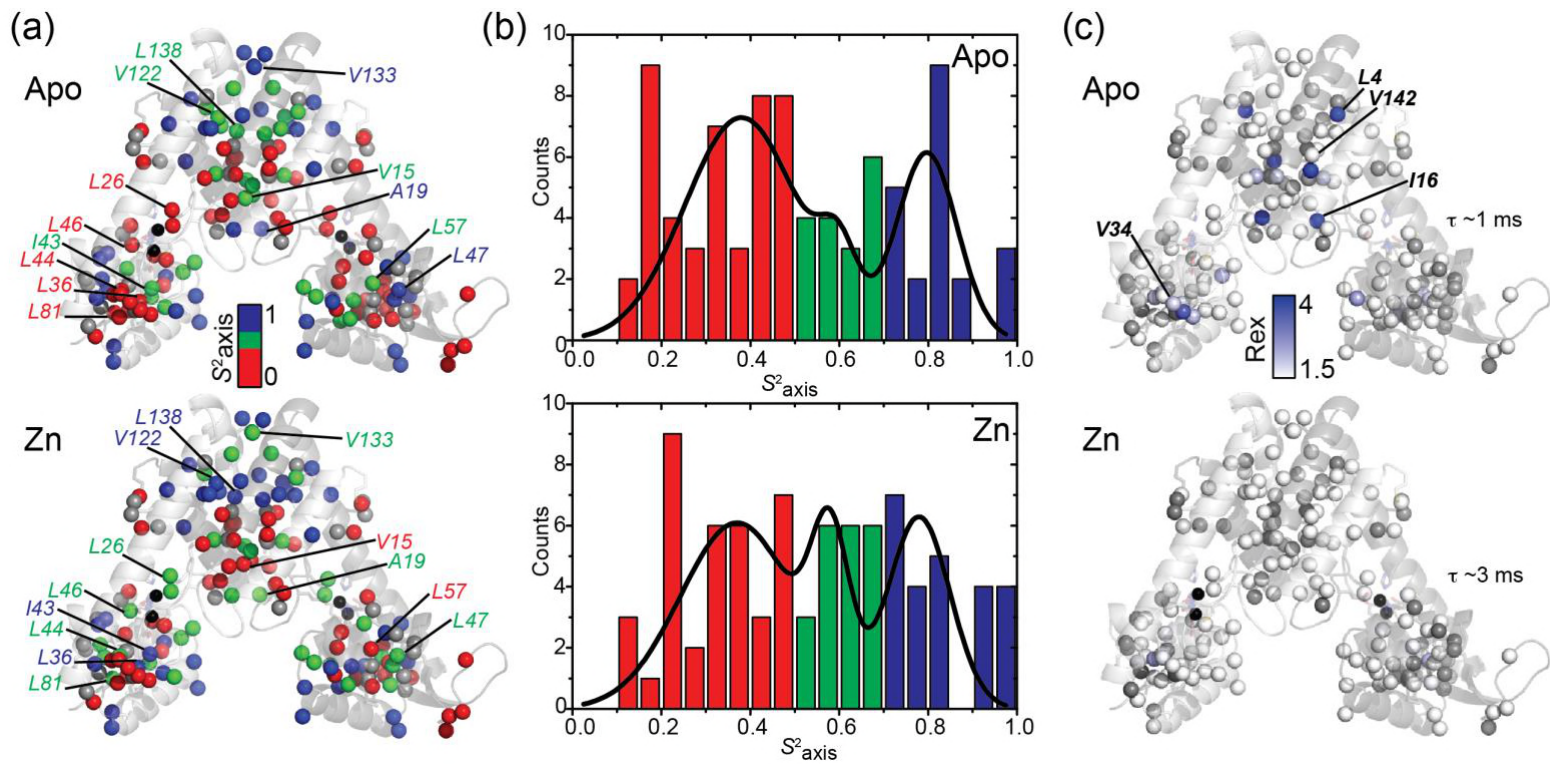
50 **Figure S2.** Small angle X-ray scattering (SAXS) analysis of AdcR in apo and Zn-binding states.
 51 (a) The Guinier region with linear fit of the scattering curve of the AdcR apo state (red) and Zn-
 52 binding state (black). Radius of gyration (R_g) of each state is presented at the low left corner.
 53 Note that scattering intensity is in arbitrary unit. (b) Dimensionless Kratky plot of the AdcR
 54 apo (red) and Zn-binding (red) state. (c) Pair distance distribution function (PDDF) of the AdcR
 55 apo (red) and Zn-binding (black) state. The end-to-end distance (D_{\max}) of apo state is 65 \AA and
 56 D_{\max} of the Zn-binding state is 75 \AA . (d) Scattering profiles of AdcR apo (red) and Zn-binding
 57 states and (e) calculated scattering profiles of crystal structures of apo ZitR^{C30AH42A} (5yi1) and
 58 Zn-binding ZitR^{E41A} (5yhz) (Zhu *et al.*, 2017) compared to the experimental and fitted curves
 59 obtained for apo-AdcR (see Fig. 2, main text).
 60



61 **Figure S3.** (a) Sequential residue-specific connectivities that link the chemical shifts of the ¹³C α
62 resonances in the α 5 helix (E107-L116; H108, H112 Zn^{II} ligands in bold) from an HNCA
63 experiment. (b), (c) ¹H, ¹⁵N NOESY-HSQC strips obtained from the same region of the α 5 helix
64 in the apo- (b) and Zn^{II} (c) states. *Right*, TALOS+ predictions in the apo- (top) and Zn^{II}
65 (bottom) states. Despite fully α -helical predictions, the apo-state is characterized by weaker *i*,
66 *i*+2 NH-NH correlations, and stronger NOEs (as solvent exchange crosspeaks) to water, relative
67 to the Zn^{II} state. This is consistent with a more highly dynamic α 5 helix in the apo-state.
68



69 **Figure S4.** Average backbone amide ^1H - ^{15}N relaxation parameters T_1 ($1/R_1$, a) and T_2 ($1/R_2$, b)
70 for the apo- (black boxes) and Zn^{II} (red boxes) states of the AdcR homodimer in different
71 regions of the molecule: DimD, dimerization domain (residues 5-20, 101-144); Zn-loop (α 1- α 2
72 loop, residues 21-37); DBD, DNA binding domain (residues 38-101, excluding the β -wing; β -
73 wing (residues 81-101). (c) Cartoon representations of the data shown in panels (a) and (b) in
74 which the two linkers that connect the two domains (middle of the α 5-helix, *dark coil*; α 1- α 2
75 loop, *light pencil*) are more dynamic in the apo-state. Note that residues analogous to the α 1- α 2
76 loop in AdcR are not observed in the crystal structure of the apo-state of *L. lactis* ZitR (Zhu *et*
77 *al.*, 2017) (see Fig. S1A), consistent with these findings in solution in apo-AdcR.
78



79 **Figure S5.** Absolute values of methyl group order parameters, S^2_{axis} (a) and R_{ex} (c) on the methyl-bearing residues. (b) Histogram plot
80 of S^2_{axis} from fitting the apo (top) and Zn^{II_2} (bottom) states in panel (a) calculated according to (Marlow *et al.*, 2010).

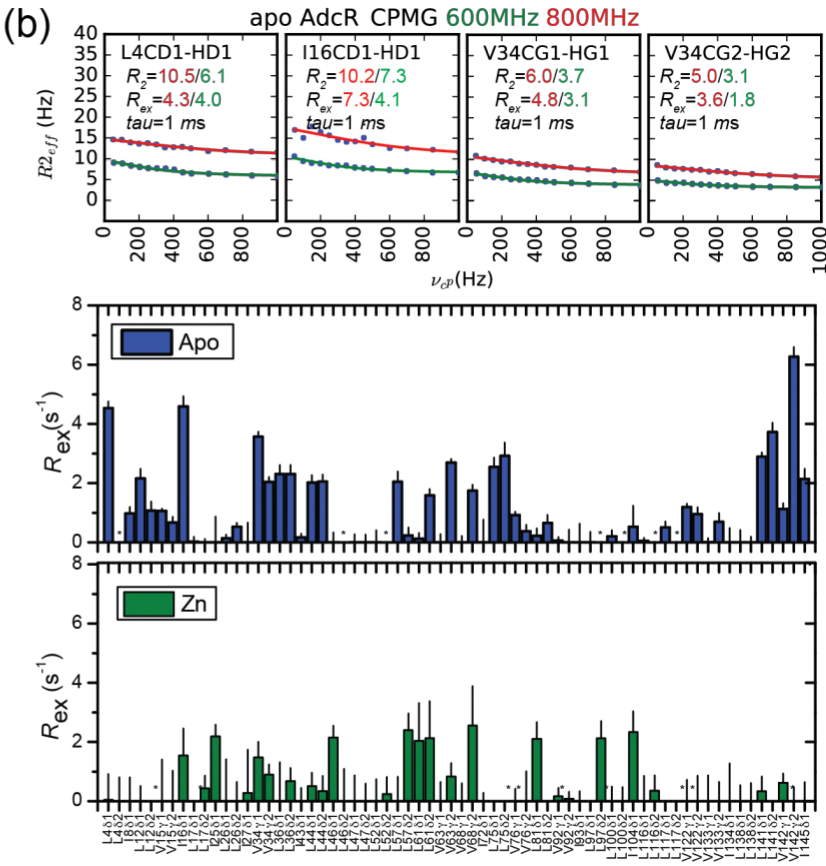
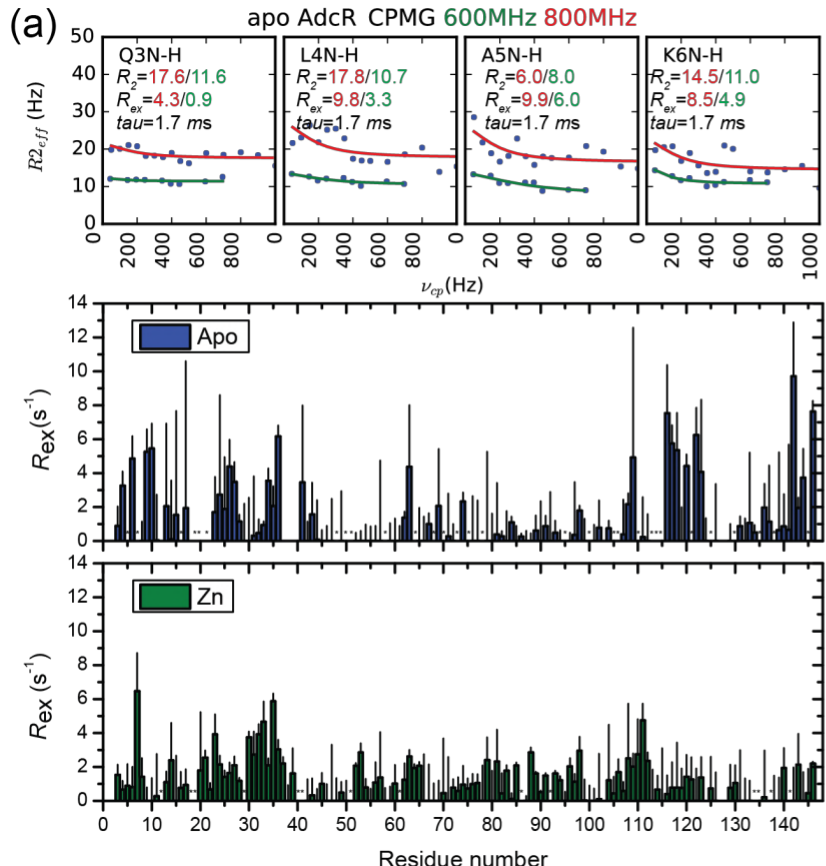
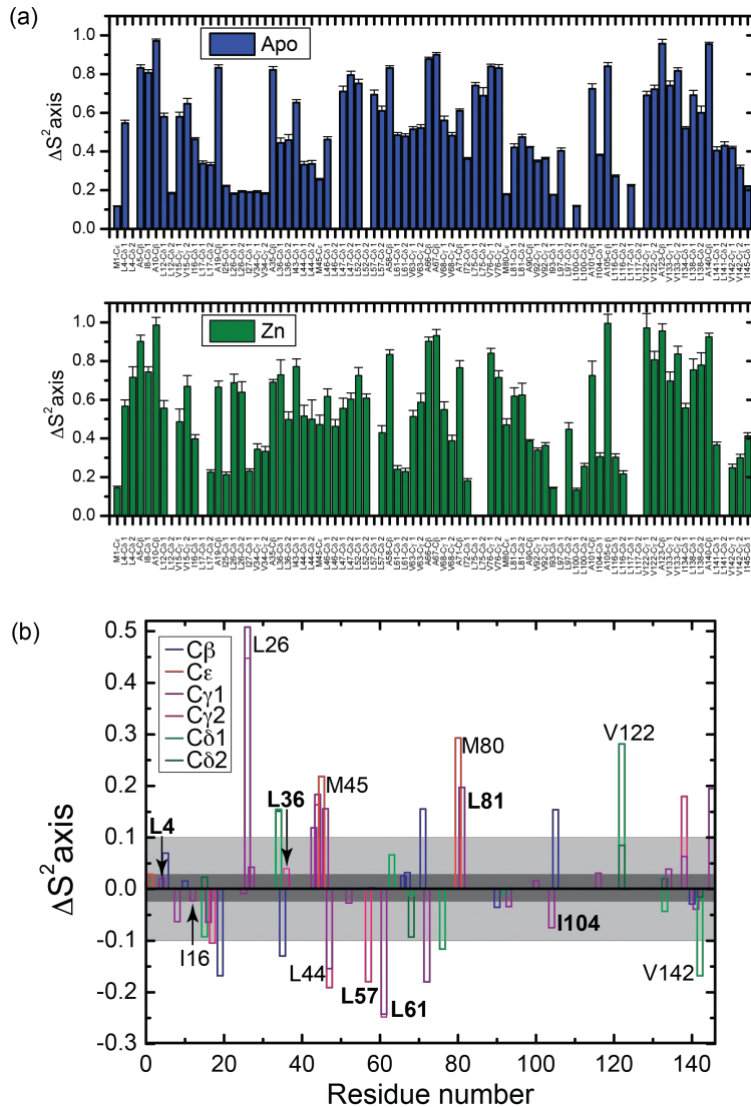
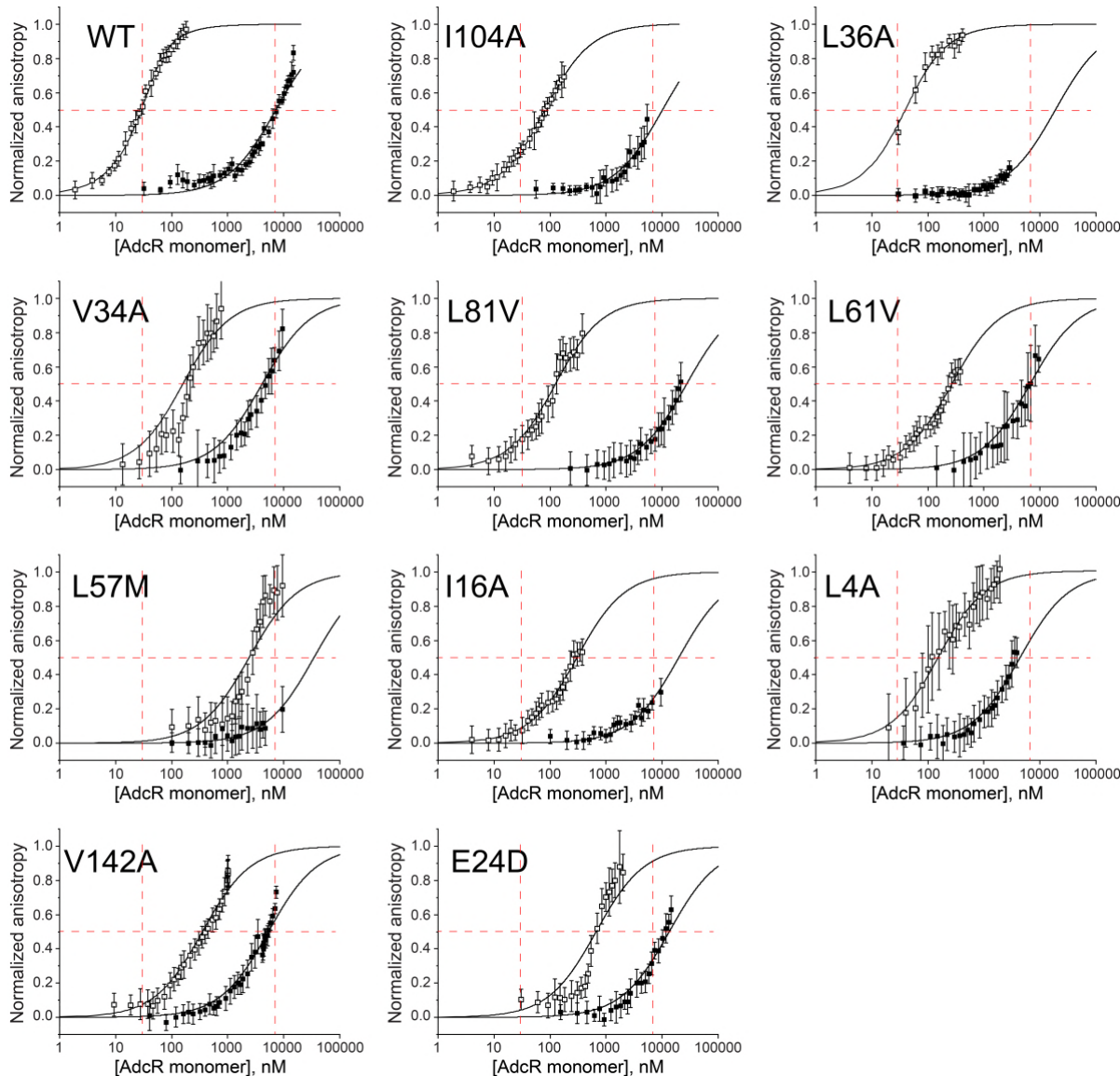


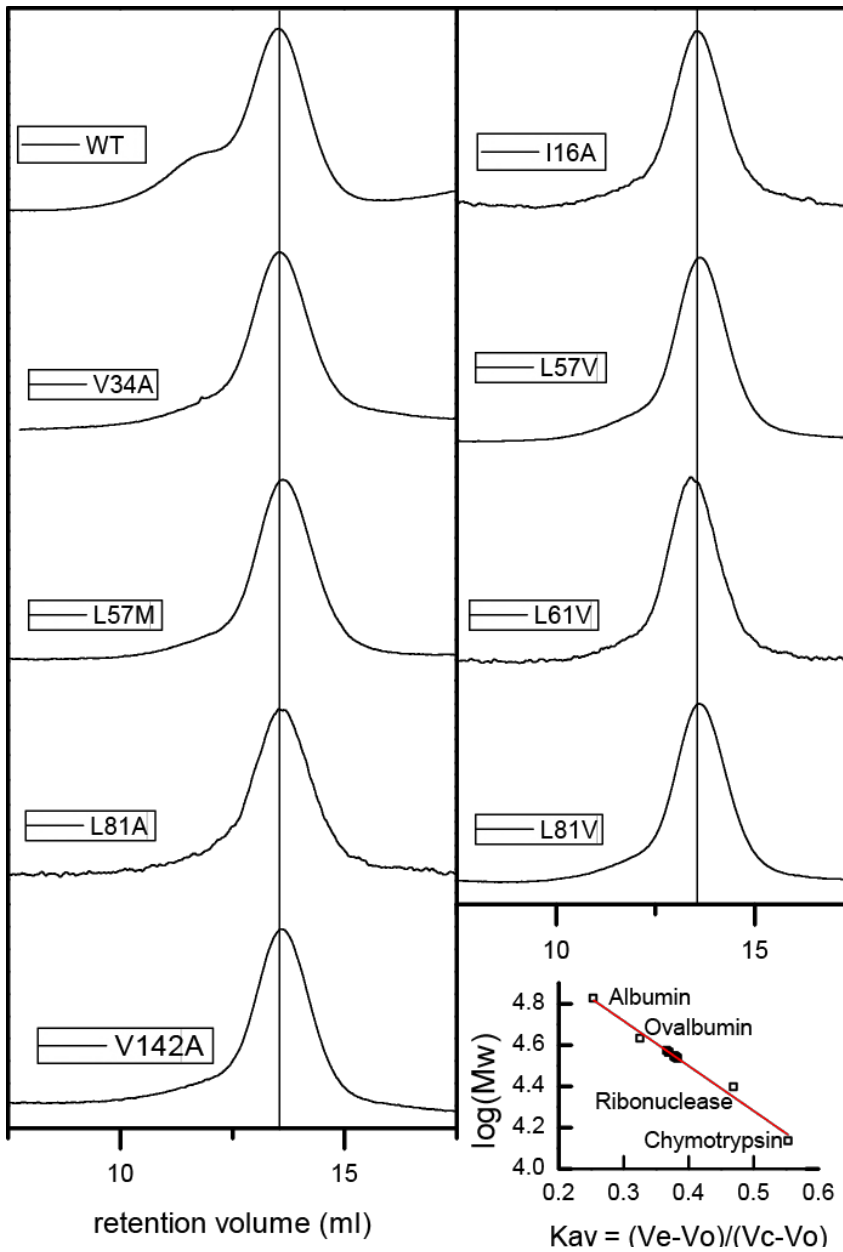
Figure S6. Representative raw relaxation dispersion curves obtained for the indicated backbone (NH) (a) or methyl group (b) used to obtain R_{ex} at 600 MHz and 800 MHz. R_{ex} for both allosteric states at 600 MHz are shown in each panel. All the residues excluded due to overlap are shown with an asterisk (Backbone Apo: 5, 7, 16, 18, 19, 22, 48, 50, 51, 58, 64, 68, 70, 73, 75, 78, 95, 100, 105, 106, 110, 113, 114, 115, 121, 125, 130, 135, 138, 145; Backbone Zn-bound: 12, 18, 19, 29, 40, 41, 51, 61, 86, 92, 134, 135, 137, 141; Sidechain Apo: L4-82, L46-82, L52-82, L97-82, L100-82, L116-82, L117-82; Sidechain Zn-bound: L12-82, L17-81, L57-81, L75-81, L75-82, L81-82, L97-81, L117-81, L117-82, L141-82).



89
90 **Figure S7.** (a) Stereospecific methyl group axial order parameters, S^2_{axis} , for apo- and $\text{Zn}^{\text{II}2}$ -
91 AdcR as measured at 600 MHz (similar results were obtained at 800 MHz; data not shown). (b)
92 Difference in axial order parameter ($\Delta S^2_{\text{axis}} = S^2_{\text{axis}}^{\text{Zn}} - S^2_{\text{axis}}^{\text{apo}}$) between apo- and $\text{Zn}^{\text{II}2}$ -states, with
93 the specific type of methyl group color-coded as indicated: $\text{C}\beta$, Ala; $\text{C}\epsilon$, Met; $\text{C}\gamma 1$, $\text{C}\gamma 2$, Val;
94 $\text{C}\delta 1$, $\text{C}\delta 2$, Leu.

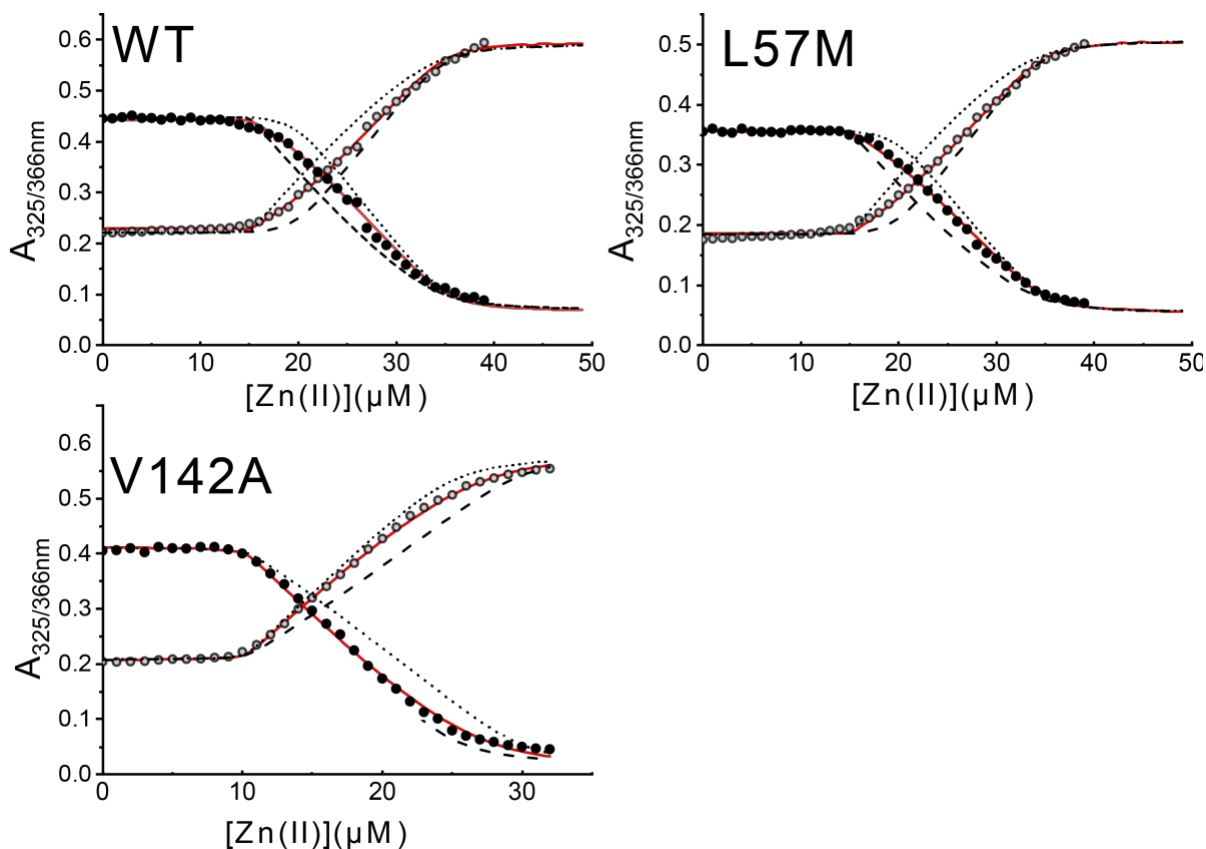


95 **Figure S8.** Representative DNA operator binding isotherms obtained for selected for wild-type
96 (WT) AdcR and selected AdcR mutants in the apo- and Zn^{II}_2 -states. The *continuous* lines
97 through each set of data correspond to nonlinear least squares fit to a 1:1 non-dissociable AdcR
98 dimer binding model, with parameters compiled in Table S2, and ΔG_c shown graphically in Fig.
99 6c (**main text**). The *red vertical and horizontal lines* represent the AdcR monomer
100 concentrations that correspond to 50% DNA-saturation points for the wild-type AdcR under the
101 same solution conditions, presented as a guide only. Conditions: 10 mM Hepes, pH 7.0, 0.23 M
102 NaCl, 1 mM TCEP (chelexed), 10 or 20 nM nM DNA, 25.0 °C with 1.0 mM EDTA (for apo-
103 AdcR) or 20 μ M Zn^{II}_2 (for Zn^{II}_2 AdcR) added to these reactions. Experiments were conducted 3
104 times for each AdcR variant.
105

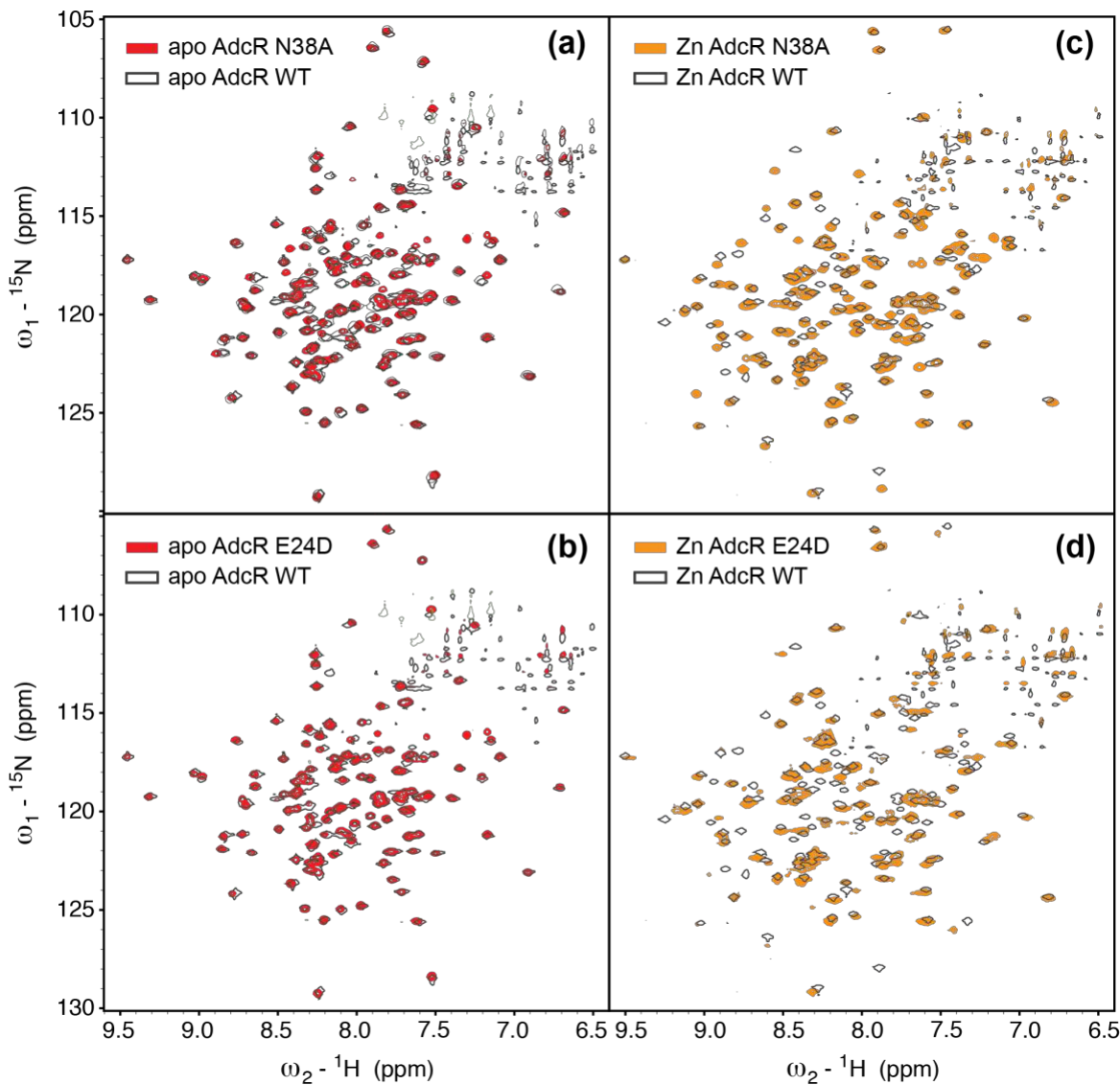


106 **Figure S9.** Gel filtration chromatograms for AdcR variants in the apo-state. *Lower right,*
107 calibration curve with standards (empty squares) and AdcR variants (filled squares).
108
109

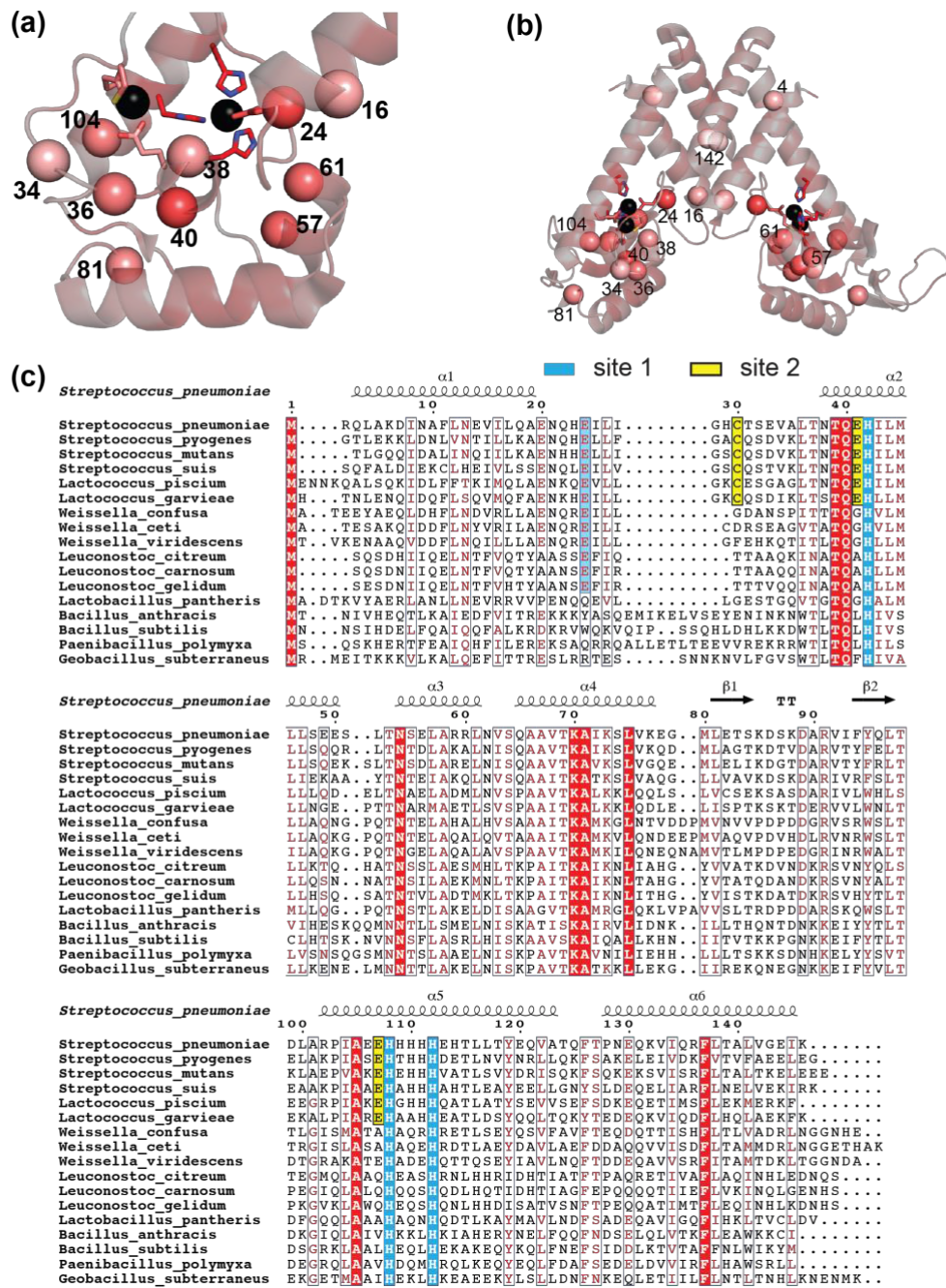
110



111 **Figure S10.** Representative Zn^{II} -binding isotherms obtained from a titration of apo (metal-free)
112 wild-type AdcR or a mutant AdcR and mag-fura-2 (mf2) with ZnSO_4 . Zn^{II} binding parameters
113 for these and other AdcRs are compiled in Table S3. Experiments were conducted 3 times for
114 each AdcR variant.
115



116 **Figure S11.** 2D ^1H , ^{15}N TROSY spectra of apo- (left) and Zn^{II_2} (right) states of N38A and E24D
117 AdcRs, compared to the wild-type AdcR (black contour; since contour line shown) acquired
118 under the same solution conditions (50 mM NaCl, pH 6.0, 35 °C).
119
120



121 **Figure S12.** Amino acid sequence conservation of *S. pneumoniae* AdcR and candidate closely
 122 related MarR family repressors. Sequence conservation highlighting those residues targeted for
 123 mutagenesis in this work with a C α sphere on the Zn II AdcR structure (Guerra *et al.*, 2011) in
 124 the DNA binding domain (a) and the entire molecule (b). The ribbon structure shows the degree
 125 of conservation by ramping the color from *white* to *bright red*, with those residues of high
 126 conservation shaded *bright red*, using Protskin (Ritter *et al.*, 2004). For reference, Zn II ligands
 127 are invariant (100% conserved). (b) Multiple sequence analysis of the 17 AdcR-like repressors
 128 used to create the sequence conservation map.
 129

130 **References**

131

132 Guerra AJ, Dann CE, Giedroc DP. 2011. Crystal structure of the zinc-dependent MarR family
133 transcriptional regulator AdcR in the Zn(II)-bound state. *J Am Chem Soc.* 133:19614-
134 19617.

135 Marlow MS, Dogan J, Frederick KK, Valentine KG, Wand AJ. 2010. The role of conformational
136 entropy in molecular recognition by calmodulin. *Nat Chem Biol.* 6:352-358.

137 Ritter B, Denisov AY, Philie J, Deprez C, Tung EC, Gehring K, McPherson PS. 2004. Two
138 WXXF-based motifs in NECAPs define the specificity of accessory protein binding to
139 AP-1 and AP-2. *EMBO J.* 23:3701-3710.

140 Sanson M, Makthal N, Flores AR, Olsen RJ, Musser JM, Kumaraswami M. 2015. Adhesin
141 competence repressor (AdcR) from *Streptococcus pyogenes* controls adaptive responses
142 to zinc limitation and contributes to virulence. *Nucleic Acids Res.* 43:418-432.

143 Zhu R, Song Y, Liu H, Yang Y, Wang S, Yi C, Chen PR. 2017. Allosteric histidine switch for
144 regulation of intracellular zinc(II) fluctuation. *Proc Natl Acad Sci U S A.* 114:13661-
145 13666.

146

